

# Observations of Outflowing UV Absorbers in NGC 4051 with the Cosmic Origins Spectrograph<sup>1</sup>

S.B. Kraemer<sup>2</sup>, D.M. Crenshaw<sup>3</sup>, J.P. Dunn<sup>4</sup>, T.J. Turner<sup>5</sup>, A.P. Lobban<sup>6</sup>, L. Miller<sup>7</sup>, J.N. Reeves<sup>6</sup>, T.C. Fischer<sup>3</sup> and V. Braitto<sup>8</sup>

## ABSTRACT

We present new *Hubble Space Telescope (HST)*/Cosmic Origins Spectrograph observations of the Narrow-Line Seyfert 1 galaxy NGC 4051. These data were obtained as part of a coordinated observing program including X-ray observations with the *Chandra*/High Energy Transmission Grating (HETG) Spectrometer and *Suzaku*. We detected nine kinematic components of UV absorption, which were previously identified using the *HST*/Space Telescope Imaging Spectrograph. None of the absorption components showed evidence for changes in column density or profile within the  $\sim 10$  yr between the STIS and COS observations, which we interpret as evidence of 1) saturation, for the stronger components, or 2) very low densities, i.e.,  $n_{\text{H}} < 1 \text{ cm}^{-3}$ , for the weaker components. After applying a  $+200 \text{ km s}^{-1}$  offset to the HETG spectrum, we found that the radial velocities of the UV absorbers lay within the O VII profile. Based on photoionization models,

---

<sup>1</sup>Based on observations made with the NASA/ESA Hubble Space Telescope, obtained at the Space Telescope Science Institute, which is operated by the Association of Universities for Research in Astronomy, Inc. under NASA contract NAS 5-26555. These observations are associated with proposal 11834.

<sup>2</sup>Institute for Astrophysics and Computational Sciences, Department of Physics, The Catholic University of America, Washington, DC 20064, USA; steven.b.kraemer@nasa.gov

<sup>3</sup>Department of Physics and Astronomy, Georgia State University, Astronomy Offices, One Park Place South SE, Suite 700, Atlanta, GA 30303, USA

<sup>4</sup>Department of Chemistry and Physics, Augusta State University, 2500 Walton Way, Augusta, Ga. 30904, USA

<sup>5</sup>Department of Physics, University of Maryland Baltimore County, Baltimore, MD 21250, USA

<sup>6</sup>Astrophysics Group, School of Physical and Geographical Sciences, Keele University, Keele, Staffordshire ST5 5BG, UK

<sup>7</sup>Department of Physics, University of Oxford, Denys Wilkinson Building, Keble Road, Oxford OX1 3RH, UK

<sup>8</sup>Department of Physics and Astronomy, University of Leicester, University Rd., Leicester, LE1 7RH, U.K.

we suggest that, while UV components 2, 5 and 7 produce significant O VII absorption, the bulk of the X-ray absorption detected in the HETG analysis occurs in more highly ionized gas. Moreover, the mass loss rate is dominated by high ionization gas which lacks a significant UV footprint.

*Subject headings:* galaxies: active – galaxies: Seyfert – galaxies

## 1. Introduction

According to the standard paradigm, Active Galactic Nuclei (AGN) are powered by accretion of matter onto a supermassive black hole. Outflowing winds may arise from an accretion disk surrounding the black hole (e.g., Rees 1987) or at larger distances. As evidence for such winds, more than 50% of Seyfert 1 galaxies, relatively local ( $z < 0.1$ ), modest luminosity ( $L_{bol} < 10^{45} \text{ergs}^{-1}$ ) AGN, show intrinsic X-ray and UV absorption (Crenshaw, Kraemer, & George 2003, and references therein), suggesting that the absorbers have global covering factors  $> 0.5$ . Blue-shifted absorption lines in their UV (Crenshaw et al. 1999), and X-ray (Kaastra et al. 2000; Kaspi et al. 2000) spectra reveal significant outflow velocities (up to  $-4000 \text{ km s}^{-1}$ ; Dunn et al. 2007). The inferred mass-loss rates are comparable to the accretion rates needed to produce the observed luminosities of AGN. Hence, mass outflows are a critical component in the structure, energetics, and evolution of AGN. Various acceleration mechanisms have been proposed for these outflows, in particular radiative driving (e.g., Murray et al. 1995), thermal winds (Begelman, McKee, & Shields 1983), and magneto-hydrodynamic flows (Blandford & Payne 1982).

Overall, there appears to be a one-to-one correspondence between X-ray and UV absorption in Seyfert galaxies (Crenshaw et al. 2003; but, see Dunn et al. 2008). Nevertheless, the nature of the physical connection between the sources of UV and X-ray absorption may vary among these objects and, indeed, among different kinematic components in individual objects. While it has been suggested that at least some of the UV absorption arises in the same gas as the X-ray absorbers (e.g., Mathur, Elvis, & Wilkes 1999), it is apparent that there is a range of physical conditions within the absorbing gas (e.g., Kraemer et al. 2002; 2003; 2005; Gabel et al. 2005). In fact, there is strong evidence that the X-ray absorbers in individual objects span a range in ionization (e.g., Steenbrugge et al. 2005; Turner et al. 2011). While there are cases in which the UV absorption lines are simply the “footprint” of the X-ray absorbers (e.g., Kraemer et al. 2005), an interesting possibility is that they are condensations in a more highly ionized medium (Kriss et al. 1996, 2000; Krolik & Kriss 2001). For example, UV and X-ray absorbers may be detected at the same radial velocities, but there is evidence, such as lower line-of-sight covering factors for the UV absorbers (Krae-

mer et al. 2006) or constraints based on photo-ionization modeling, that they are distinct physical components. If these components are indeed co-located, it raises questions about the stability of lower-ionization condensations, which may not be in pressure equilibrium with the surrounding medium (e.g. Gabel et al. 2005), and the overall dynamics of the outflows, because the integrated cross-section for absorption of radiation is significantly greater for lower ionization gas (eg., Arav, Li & Begelman 1994).

NGC 4051 is a nearby (distance = 15.2 Mpc, Russel 2004), narrow-line Seyfert 1 (NLSy1) galaxy (see Osterbrock & Pogge 1985), as evidenced by the narrowness of its  $H\beta$  emission line profile, with a full width at half maximum (FWHM)  $\approx 1070 \text{ km s}^{-1}$  (Peterson et al. 2004). Via optical reverberation mapping, Denney et al. (2009) determined the mass of the central black hole to be  $1.73_{-0.52}^{+0.55} \times 10^6 M_{\odot}$ . NLSy1s are thought to possess relatively smaller black holes than broad-line Seyfert 1s of similar luminosity, hence have higher relative mass-accretion rates and are radiating at or near the Eddington limit (e.g., Mathur 2000). Interestingly, while there is evidence that NGC 4051 is substantially sub-Eddington (see Wang & Netzer 2003), hence may not be a typical NLSy1 in that sense, it does exhibit the extreme X-ray variability characteristic of the class (e.g., Turner et al. 1999; Leighly 1999).

While observations such as those with *ROSAT* (Komossa & Fink 1997) and *ASCA* (Guainazzi et al. 1996) originally revealed the presence of intrinsic X-ray absorption in NGC 4051, it has been the subject of several more recent studies at higher spectral resolution, both in the X-ray and UV. Collinge et al. (2001) observed NGC 4051 on 2000 April 24 – 25 with the *Chandra* High Energy Transmission Grating (HETG) Spectrometer, with a total exposure time of  $\sim 81.5$  ksec, and on 2000 March 24 – 25 with the *Hubble Space Telescope (HST)*/Space Telescope Imaging Spectrograph (STIS). They found that the UV absorption showed 9 distinct kinematic components, all seen in C IV, N V, and several in Si IV, Si III, Si II, and C II, while the X-ray absorption consisted of two systems. They suggested that lower velocity X-ray system, with radial velocity  $v_r \sim -600 \text{ km s}^{-1}$ , may be connected to the UV absorbers. In *Far Ultraviolet Spectroscopic Explorer (FUSE)* spectra, obtained on 2002 March 29, 2003 January 18, and 2003 March 19, Kaspi et al. (2004) detected O VI, H I Lyman, and C III absorption consistent with the components detected by Collinge et al. In their analysis of a 100 ksec *XMM-Newton* observation from 2001 May 16-17, Krongold et al. (2007) found evidence for two X-ray absorption components. Based on time variability and photoionization modeling, they argued that both systems were within 3.5 lt-days of the central source. Steenbrugge et al. (2009; hereafter S2009) analyzed  $\sim 200$  ksec of *Chandra*/Low Energy Transmission Grating (LETG) spectrometer data, obtained 2001 December 31 – 2002 January 1 and 2003 July 23 – 24. They modeled the X-ray absorption with four components, three spanning the range of  $-200 \text{ km s}^{-1} \leq v_r \leq -610 \text{ km s}^{-1}$  and one at  $\sim -4760 \text{ km s}^{-1}$ , which could possibly be identified with the high velocity/high ionization

absorber suggested by Collinge et al. (although that system was at  $v_r \sim -2340 \text{ km s}^{-1}$ ). As with Krongold et al., Steenbrugge et al. constrained the radial distances of the X-ray components based on time variability (we will discuss this in more detail in Section 5.).

We observed NGC 4051 for 300 ksec with *Chandra*/HETG, from 2008 November 6 – 30, and for 350 ksec with *Suzaku*, on 2008 November 23. The analysis of these data are discussed in detail in Miller et al. (2010), Turner et al. (2010) and Lobban et al. (2011; hereafter L2011). To summarize the results from L2011, based on photoionization modeling and spectral analysis, we found evidence for 5 zones of absorption, spanning a range of  $-180 \text{ km s}^{-1} \leq v_r \leq -710 \text{ km s}^{-1}$  and a highly ionized zone at  $v_r \sim -5800 \text{ km s}^{-1}$ , similar to the results from S2009. Additionally, the continuum-fitting required another zone, with a covering factor of 30%. In this paper, we present our analysis of *HST* COS observations of NGC 4051. In addition to the characterization of the UV absorption, via spectral analysis and photoionization modeling, we discuss the relation between the UV absorbers and the components of X-ray absorption, the latter as modeled by L2011 and S2009.

## 2. Observations and Analysis

We obtained *HST* COS observations of the nucleus of NGC 4051 on 2009 December 11 (UT) as part of a multiwavelength effort. Due to scheduling constraints, the UV observations were not simultaneous with our *Suzaku* and *Chandra* X-ray observations. We obtained optical spectra of NGC 4051 through a  $2''$  wide slit in photometric conditions on 2009 December 17 and 18, close in time to the COS observations, with the Perkins 1.8-m telescope and DeVeny Spectrograph at Lowell Observatory. The optical spectra span the range  $4000 - 7000 \text{ \AA}$  at a spectral resolution of  $\sim 3.3 \text{ \AA}$ . We also retrieved *FUSE* archival spectra from 2002 March 29, 2003 January 18, and 2003 March 19 (Kaspi et al. 2004; Dunn et al. 2008), obtained through the  $30'' \times 30''$  aperture, and averaged these together to improve the signal-to-noise ratios (SNRs). Finally, we made use of the *HST* STIS echelle E140M observation of NGC 4051 by Collinge et al. (2001), obtained through a  $0''.2 \times 0''.2$  aperture.

We observed NGC 4051 with COS over 4 *HST* orbits with the G130M and G160M gratings through the Primary Science Aperture, which is  $2''.5$  in diameter. COS far-UV observations with these gratings are imaged onto two side-by-side detectors, and thus each observation consists of two spectra separated by a small wavelength gap (Dixon et al. 2010; Green et al. 2012). We therefore obtained the spectra at different wavelength offsets to ensure full coverage from  $1137 - 1772 \text{ \AA}$ . We give the wavelength coverages and exposure times of the individual spectra in Table 1.

We extracted the one-dimensional COS spectra from the STScI “x1d” files and interpolated them onto a common wavelength grid. The absolute fluxes of the individual spectra in the regions of overlap differ by  $<5\%$ , and we therefore combined them without any scaling in flux. We flagged regions at the ends of each spectrum that were not useful (and not flux-calibrated in the pipeline processing) as well as regions containing obvious artifacts (in particular, shadows cast by ion repeller grid wires), and then averaged fluxes in good regions on a pixel-by-pixel basis. Individual pixels in the final averaged spectrum contain contributions from one to four original spectra; most are from two spectra. The resolving power of the combined COS spectrum is  $\lambda/\Delta\lambda \approx 16,000$ , which translates to a velocity resolution of  $19 \text{ km s}^{-1}$  ( $\sim 8$  pixels) FWHM. Comparison with the STIS echelle spectra of NGC 4051 indicated a slight constant offset in the central wavelengths of the Galactic lines; we corrected for the offset by adding  $+0.07 \text{ \AA}$  to the COS spectra to allow for direct comparison with the STIS observations.

We show the full COS spectrum and identify the principal UV emission lines in Figure 1. The SNRs per resolution element range from 5 to 10 in the continuum regions and up to 50 at the peaks of the emission lines, about twice those in the STIS spectrum (for the same wavelength bins) even though the COS spectrum was obtained when NGC 4051 was in a low flux state. In Figure 2, we show the UV continuum light curve for NGC 4051 spanning 32 yr, derived primarily from *International Ultraviolet Explorer (IUE)* observations (Dunn et al. 2006). The STIS and COS observations occurred when NGC 4051 was in “average” ( $F[1365 \text{ \AA}] = 1.38(\pm 0.16) \times 10^{-14} \text{ erg s}^{-1} \text{ cm}^{-2} \text{ \AA}^{-1}$ ) and relatively low ( $F[1365 \text{ \AA}] = 0.83(\pm 0.05) \times 10^{-14} \text{ erg s}^{-1} \text{ cm}^{-2} \text{ \AA}^{-1}$ ) continuum states, respectively, although it is clear from the previous *IUE* observations that large amplitude variations could have occurred in the  $\sim 10$  yr time interval between these latest observations.

As noted by Collinge et al. (2001), the STIS UV spectrum of NGC 4051 contains a complex set of absorption lines from our Galaxy, the host galaxy of NGC 4051, and clouds of gas that are intrinsic to NGC 4051 and outflowing with respect to its nucleus. We list their absorption components, radial velocities relative to the emission-line redshift, and full-width at half-minima (FWHM; we use the same acronym for absorption and emission lines) in Table 2. In Figures 3 and 4, we show expanded versions of the COS and STIS spectra around absorption lines spanning a wide range in ionization (N V  $\lambda\lambda 1238.821, 1242.804$ ; C IV  $\lambda\lambda 1548.202, 1550.774$ ; Si IV  $\lambda\lambda 1393.755, 1402.770$ , Si III  $\lambda 1206.500$ ; C II  $\lambda 1334.532$ ; Si II  $\lambda 1260.422$ ). We also show the radial velocities of the kinematic components of absorption (for the strongest member of the doublet) in Figure 3. In order to be consistent with the radial velocities of Collinge et al., we use their systemic redshift of  $z = 0.002295$  for NGC 4051 based on its optical emission lines (de Vaucouleurs et al. 1991). Using the H I 21-cm redshift ( $z = 0.002418$ , de Vaucouleurs et al. 1991) would shift the radial velocities of the absorption

lines by an additional  $-37 \text{ km s}^{-1}$ . The higher SNRs of the COS spectrum are apparent in Figures 3 and 4, and the lower spectral resolution of COS ( $19 \text{ km s}^{-1}$ ) compared to that of the STIS E140M grating ( $7 \text{ km s}^{-1}$ ) is also clearly evident, for example in the depth of Component 1 in N V.

We find the same absorption components (G, 1– 9) in the COS spectrum that were identified by Collinge et al. (2001) in the STIS spectrum. We also confirm that Component 8, most clearly seen in N V, is shifted to more negative radial velocities in lower ionization lines (Collinge et al. suggest that this is a new low-ionization component and identify it as Component 10). We did not find any UV absorption line corresponding to the  $-2340 \text{ km s}^{-1}$  absorption system identified in X-ray observations (Collinge et al. 2001), in agreement with the lack of detection of this system in the STIS (Collinge et al.) and *FUSE* (Kaspi et al. 2004) spectra.

In Figure 4, the Galactic components (labeled “G”) in the strong low-ionization lines are completely saturated and black (i.e., consistent with zero flux in their cores), but these same lines in the COS spectra have a slight pedestal at  $\sim 6 \times 10^{-16} \text{ erg s}^{-1} \text{ cm}^{-2} \text{ \AA}^{-1}$  (about 7% of the continuum flux). The latter is likely due to instrumental scattering by the broad wings of the COS line-spread function (Dixon et al. 2010), and we take this extra emission into account when analyzing the absorption components.

### 3. Observational Results

We first identify those absorption components that are likely associated with the interstellar medium (ISM) in our Galaxy or the host galaxy of NGC 4051, based primarily on their radial velocities. Taking a closer look at Figures 3 and 4, we confirm that the “G” component identified by Collinge et al. (2001) arises in our Galaxy’s ISM; the absorption lines are broad, completely saturated at low ionization, and at a heliocentric radial velocity of only  $-39 \text{ km s}^{-1}$ . Strong Galactic lines at this velocity can also be seen in the *FUSE* spectrum of NGC 4051 (Kaspi et al. 2004); these lines, and in particular the Galactic  $\text{H}_2$  absorption, are studied in detail in Wakker (2006). Component 1 is present in N V, C IV, Si IV and possibly Si III, and is at a heliocentric radial velocity of only  $+41 \text{ km s}^{-1}$ ; it is likely a high-ionization component of gas in our Galaxy (see Bowen et al. 2008; Fox et al. 2006), although an origin in NGC 4051 cannot be ruled out. Component 8 shows broad, saturated absorption in C IV, Si IV, Si III, C II, and Si II at a central radial velocity of  $-48$  to  $-80 \text{ km s}^{-1}$  with respect to NGC 4051 (Collinge et al. 2001); it is likely due to gas in the disk or halo of NGC 4051. Component 9 shows moderate absorption in these lines as well, at a radial velocity of  $+30 \text{ km s}^{-1}$ . This component and two others seen only in  $\text{Ly}\alpha$  at

+110 km s<sup>-1</sup> and +260 km s<sup>-1</sup> (Collinge et al. 2001) are likely associated with high-velocity clouds in the host galaxy of NGC 4051, similar to those seen in our Galaxy (Fox et al. 2006; Shull et al. 2009). The remaining components are likely intrinsic to and outflowing from the active nucleus in NGC 4051.

The troughs of the low-ionization lines of Component 8 in Figure 4 are heavily saturated and go down to zero flux in the STIS data, but show excess emission in the COS data. The excess flux cannot be due to instrumentally scattered light, because it does not appear in the troughs of the nearby Galactic lines, and there is no extra line emission near the lines of Component 8, at least in the regions of Si III and Si II  $\lambda$ 1260. The Component 8 lines bottom out at  $\sim 1.2 \times 10^{-15}$  erg s<sup>-1</sup> cm<sup>-2</sup> Å<sup>-1</sup> in the COS data, rather than  $\sim 6 \times 10^{-16}$  erg s<sup>-1</sup> cm<sup>-2</sup> Å<sup>-1</sup> for the Galactic lines in the same areas of the spectrum. Thus, in addition to the instrumental scattered light, the COS spectrum show a slight excess UV continuum at the level of  $\sim 6 \times 10^{-16}$  erg s<sup>-1</sup> cm<sup>-2</sup> Å<sup>-1</sup> in its 2".5 aperture compared to the 0".2  $\times$  0".2 aperture of STIS.

Intrinsic absorption components 2 – 7 are present in N V and C IV, but none are clearly evident in Si IV or lower ionization lines, indicating that the gas in these components is relatively highly ionized. Components 2, 5, and 7 show the strongest lines, but Component 7 is strongly blended with Component 8 in C IV. The remaining components (3, 4, and 6) are relatively weak and difficult to separate from the major components due to blending. We therefore concentrate on Components 2, 5, and 7, because they are strong, less affected by blending, and likely dominate the mass outflow in the UV. We also investigate the nature of components 8 and 9 in more detail.

Convoluting the STIS spectrum with the COS line-spread function (LSF, Dixon et al. 2010) and scaling it down to match the COS fluxes, we find no clear evidence for intrinsic changes in the absorption components over the  $\sim 10$  yr interval between observations, as demonstrated for C IV in Figure 5. The apparent difference in depths of some of the absorption components is likely due to excess emission in the COS spectra, as discussed in more detail below. This is somewhat unusual, because most Seyfert 1 galaxies show strong absorption variability, including the appearance and disappearance of absorption components, on time scales of years (e.g., NGC 3516, Kraemer et al. 2002; NGC 3783, Gabel et al. 2005; NGC 4151, Kraemer et al. 2006; NGC 7469, Scott et al. 2005; Mrk 279, Scott et al. 2009; NGC 5548, Crenshaw et al. 2009; and references therein). However, this may not be too surprising, because many of the absorption lines in NGC 4051 are completely saturated (Collinge et al. 2001; this paper), and would not show detectable variations unless the ionic column densities decreased dramatically or a significant fraction of a background emission source (e.g., the broad line region) was covered or uncovered (e.g., see Crenshaw et

al. 2004) over the 10-year interval between STIS and COS observations. Thus, we cannot rule out ionic column density changes in the saturated lines between the STIS and COS observations.

To further investigate the nature of the uncovered emission in the COS spectrum and its effect on measurements of the ionic column densities, we generated a detailed model of the background emission spectrum. We fitted a spline to the continuum across the entire spectrum using regions unaffected by emission or absorption features. To generate template profiles for the emission lines, we used the He II  $\lambda 1640$  line, which is not affected by absorption. Inflections in the He II profile, shown in Figure 6, suggest the presence of 3 components: broad, intermediate, and narrow. We fitted the broad component with a cubic spline and the other two components with Gaussians. The resulting widths of the emission-line components are 260, 1090, and 4500  $\text{km s}^{-1}$  (FWHM). We associate the first and last of these with the narrow-line region (NLR) and broad-line region (BLR), and suggest that the middle component arises in an “intermediate-line region” (ILR), which we have also identified in low-flux UV spectra of NGC 4151 (Crenshaw & Kraemer 2007) and NGC 5548 (Crenshaw et al. 2009). However, we note that our “ILR” likely corresponds to the “BLR” detected in optical spectra, which show a “broad” component of  $\text{H}\beta$  with  $\text{FWHM} = 1070 \text{ km s}^{-1}$  (Peterson et al. 2004).

To model the emission-line profiles of the high-ionization lines, we reproduced the He II templates at the expected positions of the lines, retaining the same velocity widths, and scaled them in intensity to obtain the best fits to the observed profiles.. Allowing the doublet ratios (e.g., N V  $\lambda 1238.8/\lambda 1242.8$ ) to vary between 1 and 2 (see Crenshaw et al. 2009) made little difference to the overall fits, so we fixed them to a value of 1. We adopted the minimum narrow-line fluxes needed to fit the observed profiles. Figure 7 shows that our procedure yields an excellent fit to the observed profiles in the COS spectra, and provides an accurate deconvolution of the NLR, ILR, and BLR contributions to the emission-line profiles.

As noted above, absorption components 2, 5, and 7 are saturated at zero flux in their cores in the STIS spectra. Their non-zero fluxes in the COS spectra must be due to uncovered emission. To model the uncovered emission, we use our derived values for the instrumentally-scattered light and the excess emission from the host galaxy, plus contributions from the NLR fluxes derived above, as we have done in the past (Kraemer et al. 2002; Crenshaw et al. 2009). Thus, a reasonable model for the uncovered emission is a combination of the excess continuum flux at a level of  $1.2 \times 10^{-15} \text{ erg s}^{-1} \text{ cm}^{-2} \text{ \AA}^{-1}$  (half due to instrumental light, half to extra UV flux in the COS aperture) plus the NLR emission. As shown in Figure 6, the model provides provides a reasonably good fit to the uncovered emission, in that it



skirts just beneath the unblended saturated lines associated with Components 2, 5, and 7. Furthermore, it demonstrates that Component 5 and 7 must be mostly inside the NLR, whereas Component 8 absorbs most, if not all, of the NLR emission (we cannot constrain Component 2 in this manner because it does not overlap the NLR emission in velocity space). On the other hand, Components 2, 5 and 7 absorb most, if not all, of the continuum, BLR, and ILR emission, and therefore lie outside of these regions.

We measured the ionic column densities of Components 2, 5, 7, 8, and 9 by subtracting the uncovered emission components from the spectra and dividing by the covered emission components (covered continuum, BLR, and ILR fluxes) to obtain normalized profiles. We then converted these to optical depth as a function of wavelength, and integrated across the optical depth profiles to obtain column densities (Crenshaw, Kraemer, & George 2003). Uncertainties in the measured column densities come from propagation of photon noise and different reasonable fits to the underlying emission. Measurements of unsaturated lines in both COS and STIS spectra resulted in differences smaller than the quoted uncertainties, reinforcing our claim that these absorption features did not vary. Components 2, 5, and 7 are completely saturated in N V and C IV, and we can only provide lower limits to their ionic column densities. We used the higher SNR COS spectra, and assumed the least amount of uncovered emission, given the uncertainties, to determine these limits. To obtain upper limits to the Si IV columns, we added model absorption-line profiles to the spectra and decreased their equivalent widths until they were not detectable above the noise.

We used the *FUSE* spectra of NGC 4051 to obtain further constraints on the ionic column densities. The COS and *FUSE* observations are not concurrent, and our underlying assumption is that the limits obtained from the COS observations apply to the epochs of *FUSE* observations as well. By matching the COS and average *FUSE* spectra in the region of wavelength overlap, we find the continuum flux at 1365 Å is  $1.06 \times 10^{-14}$  erg s<sup>-1</sup> cm<sup>-2</sup> Å<sup>-1</sup> projected from the *FUSE* spectra, intermediate between the STIS and COS observations, providing further justification for the above assumption. As noted by Kaspi et al. (2004), the O VI absorption components are blended together into big troughs, similar to Ly $\alpha$ , and no useful limits can be obtained. We agree with Kaspi et al. that N III  $\lambda$ 989.790 absorption is undetectable, primarily due to contamination by geocoronal emission and Galactic H<sub>2</sub> absorption, and that C III  $\lambda$ 977.020 absorption is present in Component 5 and possibly present in Component 2 (Component 7, if present, is blended with 8). We see no evidence for P V  $\lambda$ 1117.98, 1128.01 absorption, which would have indicated very high columns of high-ionization gas, nor C III\*  $\lambda$ 1175 absorption in either the *FUSE* or *COS* spectra. As noted by Kaspi et al., H I Lyman absorption lines are seen extending down to the Lyman edge. We identified H I absorption to Ly6  $\lambda$ 930.748 in Component 2 and Ly9  $\lambda$ 920.963 in Component 5, whereas Lyman absorption in Component 7 is always blended with that

in Component 8. The longer wavelength lines of Ly $\beta$  and Ly $\gamma$  are strongly affected by geocoronal emission and likely saturated in any event, so we used the shorter wavelength lines to determine the H I columns for Components 2 and 5. The C III absorption profiles for Components 2 and 5 (shown in Kaspi et al. 2004) appear not to be saturated, and we measured their columns directly by integrating their optical depths across the profiles after subtracting off the uncovered emission.

We present the ionic column densities or limits for Components 2, 5, 7, 8, and 9 in Table 3. Using a different technique for the *FUSE* analysis, Kaspi et al. (2004) found that the H I column density in Component 5 is  $1.0_{-0.5}^{+0.6} \times 10^{16} \text{ cm}^{-2}$ . Our value is about half of theirs, but the error bars still overlap. They do not give column densities for any of the other lines. We do not detect O I in any absorption component; its ionic column density is therefore  $< 1.0 \times 10^{14} \text{ cm}^{-2}$ .

To gauge the reddening in the line of sight to the nucleus of NGC 4051, we measured the total fluxes of the He II  $\lambda 1640$  emission line in the COS spectrum and the He II  $\lambda 4686$  emission line in the concurrent optical spectra. The lines are due to recombination and the intrinsic H II  $\lambda 1640/\lambda 4686$  ratio should be  $\sim 7.25$ , for an electron density  $n_e = 10^6 \text{ cm}^{-3}$  and temperature  $T = 5 \times 10^4 \text{ K}$  (Seaton 1978), which we chose to match the combined BLR and NLR emission. To ensure an accurate absolute flux, we scaled our averaged optical spectrum slightly (by a factor of 1.15) so that our [O III]  $\lambda 5007$  flux matched the well-established value of Peterson et al. (2000). The resulting observed He II  $\lambda 1640/\lambda 4686$  ratio is then  $(14 \times 10^{-14} \text{ erg s}^{-1} \text{ cm}^{-2}) / (4.0 \times 10^{-14} \text{ erg s}^{-1} \text{ cm}^{-2}) = 3.5$ . This value yields  $E(B-V) = 0.19$  (only 0.01 from our Galaxy) for a Galactic reddening curve (Savage & Mathis 1979) and  $N_H = 1.0 \times 10^{21} \text{ cm}^{-2}$  for a standard Galactic dust-to-gas ratio (Shull & van Steenberg 1985). Kaspi et al. (2004) present an observed spectral energy distribution (SED) for NGC 4051 which has a UV spectral index of  $\alpha = -2.0$  (where  $F_\nu = K\nu^\alpha$ ) between 1160 and 3000 Å. Correction for extinction based on the above reddening yields  $\alpha = -1.3$  and  $F(1365 \text{ Å}) = 6.4 \times 10^{-14} \text{ erg s}^{-1} \text{ cm}^{-2} \text{ Å}^{-1}$  for the STIS observation used in Kaspi et al.'s SED.

We searched for and did not find any H<sub>2</sub> absorption in the *FUSE* spectrum near the redshift of NGC 4051. Using the methods of Dunn et al. (2007), we find that  $N(\text{H}_2) < 5.0 \times 10^{14} \text{ cm}^{-2}$  for any rovibrational level. Thus, the reddening is not due to dust in cold molecular gas.

## 4. Photoionization Models

The photoionization models used for this study were generated using the photoionization code Cloudy, version 08.00 (last described by Ferland et al. 1998). We assumed an open, or “slab”, geometry. As per convention, the models are parametrized in terms of the dimensionless ionization parameter,  $U = Q/(4\pi r^2 c n_{\text{H}})$ , where  $r$  is the radial distance of the absorber,  $n_{\text{H}}$  is hydrogen number density, in units of  $\text{cm}^{-3}$  and  $Q = \int_{13.6\text{eV}}^{\infty} (L_{\nu}/h\nu) d\nu$ , or the number of ionizing photons  $\text{s}^{-1}$  emitted by a source of luminosity  $L_{\nu}$ , and the total hydrogen column density,  $N_{\text{H}}$  (in units of  $\text{cm}^{-2}$ ), where  $N_{\text{H}} = N_{\text{HI}} + N_{\text{HII}}$ .

### 4.1. Model Inputs

In our previous paper (L2011), we characterized the intrinsic X-ray continuum in the *Suzaku* XIS + HXD (0.5 – 10 keV and 20 – 50 keV, respectively) as a power-law with a photon index  $\Gamma \approx 2.5$ . This is consistent with constraints on the EUV-soft X-ray SED obtained via photoionization models and the ratios of [Ne V] 14.32  $\mu\text{m}$ , 24.32  $\mu\text{m}$ , [Ne III] 15.56  $\mu\text{m}$ , and [O IV] 25.89  $\mu\text{m}$  observed in *Spitzer* IRS spectra (Meléndez et al. 2011). Noting that the UV observations found NGC 4051 in a relatively low-flux state, we used the lowest of the 3 *Suzaku* fluxes,  $3.4 \times 10^{-12} \text{ ergs cm}^{-2} \text{ s}^{-1}$  at 2 keV, corrected for absorption, and extrapolated down to 1365 Å, assuming a spectral index  $\alpha = 1.5$ . This predicts a flux of  $7.4 \times 10^{-14} \text{ ergs cm}^{-2} \text{ s}^{-1} \text{ \AA}^{-1}$ , which is close to the dereddened flux from the STIS spectrum used by Kaspi et al. (2004). Based on this, and the fit to the UV continuum (see Section 3), we have parametrized the SED in the form of a broken power law, such that  $L_{\nu} \propto \nu^{\alpha}$  as follows:  $\alpha = -1.3$  for energies  $< 9.8 \text{ eV}$  (1365 Å),  $\alpha = -1.5$  over the range  $9.8 \text{ eV} \leq h\nu < 50 \text{ keV}$ <sup>1</sup>. We included a low energy cut-off at 0.1 eV and a high energy cutoff at 100 keV. Using this SED and the unabsorbed flux at 2 keV, we determined that  $Q \approx 6.4 \times 10^{52} \text{ photons s}^{-1}$ . For these models, we have assumed roughly solar elemental abundances (e.g., Asplund et al. 2009) as follows (in logarithm, relative to H, by number): He:  $-1.00$ , C:  $-3.57$ , N:  $-4.17$ , O:  $-3.31$ , Ne:  $-4.07$ , Na:  $-5.76$ , Mg:  $-4.40$ , Al:  $-5.55$ , Si:  $-4.49$ , P:  $-6.59$ , S:  $-4.88$ , Ar:  $-5.60$ , Ca:  $-5.66$ , Fe:  $-4.50$ , and Ni:  $-5.78$ .

In these spectra, we were only able to derive column densities for a small number of ions in the various kinematic components (see Section 3 and Table 3). Therefore, our modeling method is to fit these derived columns, within the measurement uncertainties, exceed lower

---

<sup>1</sup>In L2011, the photoionization models were parametrized in terms of  $\xi = (\int_{13.6\text{eV}}^{13.6\text{keV}} L_{\nu} d\nu)/(n_{\text{H}}r^2)$ ; for our assumed SED,  $U \approx 0.04 \times \xi$ .

limits for the saturated lines, and under-predict upper limits for those ions which were not detected. To achieve this, we used the “optimize” command in Cloudy, adjusting the commandable errors as needed to improve the fit (see Cloudy Manual, HAZY; Ferland 1996). However, uncertainties in both elemental abundances and atomic data (e.g., dielectronic recombination rates) can affect the predictions of ionic column densities, particularly for poorly populated ionic states. The final model parameters for the strongest absorption components and the predicted ionic column densities are listed in Tables 4 and 5, respectively.

## 4.2. Model Results

As discussed in Section 2, components 2 – 7 are associated with mass outflow, while components 8 and 9 are more likely formed in the ISM or halo of the host galaxy. Of the mass-outflow components detected in the STIS and COS spectra, the strongest are components 2, 5, and 7. For components 2 and 5, we have measured column densities for H I and C III (see Table 3), lower limits for N V and C IV, and an upper limit for Si IV. Given these limited constraints, models spanning a range of  $U$  and  $N_{\text{H}}$  can fit the measured values. For example, using the measured columns for H I and C III and their respective uncertainties, and the lower limit for C IV, acceptable model parameters for component 5 are  $\log U = -0.45_{+0.1}^{-0.2}$  and  $\log N_{\text{H}} = 20.74_{+0.25}^{-0.40}$ . However, for component 5,  $v_r = 268 \text{ km s}^{-1}$  and  $\text{FWHM} = 133 \text{ km s}^{-1}$ , which are quite close to the values determined by S2009 for their zone 4, i.e.,  $v_r = 270 \text{ km s}^{-1}$  and  $\text{FWHM} = 170 \text{ km s}^{-1}$ . Furthermore, the S2009 zone 4 model parameters,  $\log U = -0.64$  and  $\log N_{\text{H}} = 20.4$ , are within the range acceptable for component 5, hence we have opted to use these values. The predictions for this model are a good fit for component 5, albeit with a slight overprediction of the C III column density. To summarize, while our final model parameters could be off by 0.2dex in  $U$  and 0.4dex in  $N_{\text{H}}$ , requiring consistency with the X-ray results can, at least, direct us to a preferred location in  $U$ - $N_{\text{H}}$ -space (we discuss the relationship between the UV and X-ray absorption in detail in Section 5).

For component 2, there are no clear X-ray constraints and our best-fit model overpredicts the H I column density and slightly underpredicts the lower limits for N V and C IV. Naïvely, one might assume that this is an indication of super-solar N/H and C/H ratios. Although that cannot be ruled out, increasing the carbon abundance results in a factor of  $\gtrsim 2$  overprediction of C III. The physical parameters of component 7 are even less well-constrained by the observations, because only lower limits for C IV and N V and an upper limit for Si IV can be determined, and other ions, including H I, are blended with component 8. However, we are able to fit the available constraints using model parameters adapted from

zone 2 (L2) in L2011.

As shown in Figures 3 and 4, while there is N V and C IV absorption spanning the velocities of components 7 and 8, the lower ionization lines, e.g., C II, Si III and Si II, appear to be associated primarily with component 8. This is consistent with our parametrization for component 7, since our model predicts column densities for these ions  $N_{\text{ion}} < 10^{12} \text{ cm}^{-2}$ . In Figure 3, the C IV line is saturated for component 8, N V is weak, and Si IV is strong, but not saturated. On the other hand, C II, Si III, and, possibly, Si II appear saturated, and at a more positive radial velocity than the high-ionization lines, which is why there were identified as a separate component (10) in Collinge et al. (2001). This suggests that there are two physical sub-components near this velocity. One other constraint is that there is no detectable C II\*, which we find requires that  $N_{\text{CII}^*} < 1.3 \times 10^{13} \text{ cm}^{-2}$ . Using the ratio of the upper limit to the column density for C II\* to the lower limit for C II (see Table 4), we obtain an electron density  $n_e \approx 1 \text{ cm}^{-3}$ , for an electron temperature  $T_e = 8 \times 10^3 \text{ K}$  (e.g., Srianand & Petitjean 2000); the density must be somewhat lower than this value, since it was estimated using the lower limit for  $N_{\text{CII}}$ . For the lower ionization model, 8L, with  $n_H = 0.36 \text{ cm}^{-3}$ ,  $\log U = -3.5$  and  $\log N_H = 18.8$ , we were able to match the  $N_{\text{CII}^*}$  constraint and obtain acceptable predictions for the column densities or lower limits for C II, Si III, Si II, Fe II. For the higher ionization component, 8H, we were able to match  $N_{\text{NV}}$ , within the uncertainties, and obtained a reasonable fit for  $N_{\text{SiIV}}$  with  $\log U = -2.4$  and  $\log N_H = 19$ , which requires that  $n_H = 0.03 \text{ cm}^{-3}$ , if the two sub-components are co-located. Based on the model parameters and our estimate of  $Q$ , component 8 is  $> 12.5 \text{ kpc}$  from the AGN, hence, possibly in the halo of the host galaxy. Note, this is a larger radial distance than that found for the similar low-density, low-ionization components, A and C, in NGC 4151, which were determined to be at radial distances of 681 pc and 2.15 kpc, respectively (Kraemer et al. 2001). Finally, component 9 shows only weak C IV and lower-ionization ions (Table 3). We obtained a reasonable fit, save the over-prediction of Si III, which could be due to uncertainties in third-row element dielectronic recombination rates (e.g., Ali et al. 1991). As with component 8, the absence of CII\* suggests a low density. Assuming the same  $n_H$  as for 8L, component 9 would be 19.3 kpc from the AGN.

Our models for components 2, 5, and 7 predict  $N_{\text{OVI}} > 10^{16} \text{ cm}^{-2}$  (see Table 5). To test whether the predictions are consistent with the data, we plotted the normalized flux for O VI as a function of velocity, using the measured values of FWHM and  $v_r$  for each of the three components. As shown in Figure 8, the combined profile is characterized by a deep, square trough, spanning velocities  $-700 \text{ km s}^{-1} \lesssim v \lesssim 0 \text{ km s}^{-1}$ , in good agreement with the *FUSE* O VI  $\lambda 1032$  profile presented in Kaspi et al. (2004; see their Figure 3), except for the presence of some uncovered emission in the latter. However, while our UV model predictions are consistent with the observed O IV absorption, we cannot rule out

the presence of additional absorption over this range in velocity, as may be present in more highly ionized gas (i.e., the X-ray absorbers).

None of the component models predict  $N_{\text{H}} > 2.5 \times 10^{20} \text{ cm}^{-2}$ . Coupled with their relatively high values of  $U$ , one consequence of the low column densities is that none of the three strongest components is sufficiently optically thick to the ionization radiation to justify including the effects of screening by intervening absorbers, e.g. as is the case in NGC 3516 (Kraemer et al. 2002; Turner et al. 2005) and NGC 4151 (Kraemer et al. 2001; 2005; 2006). Also, while, as noted in Section 3, the continuum and BLR emission is reddened, consistent with an intervening column of  $N_{\text{H}} = 1.0 \times 10^{21} \text{ cm}^{-2}$  of dusty gas, none of the models for the UV absorber components has a sufficient column density to account for the reddening. In fact, the sum of the column densities of components 2, 5, 7, 8, and 9 is only  $5.4 \times 10^{20} \text{ cm}^{-2}$ . Furthermore, the presence of Fe II in component 8, along with the likelihood, confirmed by our photoionization model, that most of the iron is in the form of Fe III, hence not detectable in these spectra, indicates that there is very little depletion of iron onto dust grains. Hence, there cannot be a significant amount of dust in this component. One possibility is that the dust is distributed within components 2, 5, and 7, and that additional dust exists in the higher ionization gas. However, there are no tight constraints from the modeling of the UV or X-ray absorption (e.g. L2011) that can provide a definitive answer, hence we must leave the question as to origin of the reddening open.

## 5. Physical Properties of the Absorbers

### 5.1. Connection with the X-ray absorbers

As shown in Table 5, the models for UV components 2, 5, and 7 predict  $N_{\text{OVII}} > \text{several} \times 10^{16} \text{ cm}^{-2}$ . Hence, these components may be detectable in the HETG spectra. On the other hand, the UV component models all predict  $N_{\text{OVIII}} < 10^{16} \text{ cm}^{-2}$ , which suggests the presence of more highly ionized gas without a strong UV “footprint”. In order to compare the X-ray and UV absorption in detail, we first compared the kinematic profiles of strong absorption lines, specifically O VII and O VIII with N V and C IV. Initially we found no overlap of velocities, because the X-ray absorption lines are offset to more negative velocities than the UV. However, this velocity offset is likely due to the calibration of the *Chandra* gratings (see the *Chandra* Proposer Guide: <http://cxc.harvard.edu/proposer/POG/html/HETG.html>). For example, in L2011, we had used only the MEG in the 0.5-1.0 keV regime. The accuracy of the wavelength scale for MEG is  $\pm 0.011 \text{ \AA}$ . Hence, for O VII, this yields absolute uncertainty in velocity of  $\pm 150 \text{ km s}^{-1}$ , while for Ne IX it would be  $\pm 235 \text{ km s}^{-1}$ . For Si XIII, we used the MEG and HEG combined. For the HEG, the accuracy of the wavelength scale

is  $\pm 0.006 \text{ \AA}$ , which results in an uncertainty for Si XIII of  $\pm 250 \text{ km s}^{-1}$ . This justifies some flexibility in comparing the X-ray and UV line kinematics. Indeed, after we applied a  $+ 200 \text{ km s}^{-1}$  shift to the X-ray spectra, we found visual correlation between the UV and X-ray absorption, as shown in Figure 9. The trough of the O VII profile encompasses UV components 2 through 8, and, while the deepest part of O VIII profile covers UV components 1 through 5, there is significant O VIII absorption blueward of component 1.

In L2011, we determined there were 6 separate zones of absorption. The highest velocity zone, at  $v_r \sim -0.02c$ , in which H and He-like Fe lines form, is too highly ionized to produce detectable UV lines and, in fact, no UV absorption is detected at this velocity. And, as we have found in previous studies (e.g. Turner et al. 2005), no lines are detected from the high-ionization, high-column, partial-covering zone. For the remaining zones, we list the model parameters, with  $U$  given for the equivalent  $\xi$ , and possible associated UV components, in Table 6.

The two lower ionization X-ray absorbers, zones L1 and L2, should produce strong UV signatures. With our velocity correction to the *Chandra* spectra, L1 and L2 should be near the systemic velocity, which would associate them, kinematically, with UV components 7, 8, and 9. As we noted above, a model using  $U$  and  $N_{\text{H}}$  corresponding to zone 2 provides a good match to UV component 7, which suggests that these indeed are the same component. Given that, one would expect that L1 is associated with UV components 8 and 9. However, the column density determined by L2011 for L1 is  $\sim 30$  times larger than that of our models 8L, 8H and 9 combined. Furthermore, using the parameters for L1 ( $\log U = -2.25$ ,  $\log N_{\text{H}} = 20.4$ ), a Cloudy-generated model predicts heavily saturated Si IV, with  $\log N_{\text{SiIV}} > 15$ , of which there is no evidence in the STIS and COS spectra. Therefore, while we find significant absorption near systemic, in agreement with the HETG analysis, the column density derived from the UV analysis is much smaller than that derived from the X-ray. The source of the discrepancy may be the uncertainty in the strength of the  $\sim 0.1 \text{ keV}$  black-body component used in the parametrization of the HETG data. If the black-body were weaker than assumed, the continuum fitting would require less low-ionization absorption. For example, if we leave the black-body in the spectrum, but allow its normalization to adjust, we find a 90% lower limit on the column of zone L1 of  $\log N_{\text{H}} > 19.47$  which would be in better agreement with UV components 8 and 9. The other zones (L2-L4) are unaffected, as they are well constrained by the strong absorption lines in the spectrum. However, although the exact form of this emission is uncertain, removing the black-body component completely leads to an unacceptable fit to the data.

L2011’s zones L3a and L3b are significantly more ionized than the modeled UV components (see Table 6), hence they do not predict any significant UV absorption. However,

it is possible that the absorbers are inhomogeneous, i.e., part of a multi-phase wind (e.g., Krolik & Kriss 2001; Chelouche & Netzer 2005) and each kinematic component included gas of a range of ionization/density. As such, it is conceivable that L3a and UV component 4, L3b and UV component 1, and L4 and UV component 2 are associated. The weak N V and C IV detected in component 1 and 4 may arise in small, dense knots within the higher ionization gas. For component 2, the predicted  $N_{\text{OVII}}$  is much smaller than for L4, which, again, suggests embedded low ionization gas.

As noted above, S2009 used a 4 zone model for the absorbers in their analysis of the LETG spectrum of NGC 4051 (we will refer to their zones as S1-4). As discussed in L2011, there is rough agreement between S2009’s high velocity component, S4, and the highest velocity component in the HETG analysis. The model parameters for the three lower-velocity zones are listed in Table 6. S3 is at roughly the same  $v_r$  and has similar  $U$  and  $N_{\text{H}}$  as L3b. In terms of  $U$  and  $N_{\text{H}}$ , the best agreement across the three data-sets is for UV component 7, L2, and S1. However, both L2011 and S2009 claim much larger velocity dispersions than permitted by the FWHM of the UV lines. One possibility is that a nearby weaker UV component, in this case component 6, contributes to the X-ray absorption. To illustrate this, in Figure 10 we show a simulation of the case of two absorber components at the velocities of 6 and 7, assuming  $\tau = 10$  in their cores. When the profiles are smoothed to the velocity resolution of the LETG,  $\sim 300 \text{ km s}^{-1}$ , we obtain a FWHM  $\sim 250 \text{ km s}^{-1}$ , similar to that determined for S1. To further explore this, we generated a model for UV component 6, with  $\log U = -0.08$  and  $\log N_{\text{H}} = 20.0$ , which predicts  $N_{\text{NV}} = 5.0 \times 10^{13} \text{ cm}^{-2}$ , compared to the measured value of  $N_{\text{NV}} = 5.0 (\pm 2.0) \times 10^{13} \text{ cm}^{-2}$ , and  $N_{\text{OVII}} \sim \text{several} \times 10^{16} \text{ cm}^{-2}$ , similar to L2011’s model for L2. Hence, the broad O VII suggested by the fit for S1 and L2 is consistent with similar contributions from UV components 6 and 7.

Although there is general agreement between the UV components and the results of the two X-ray analyses, there are some clear discrepancies. First, although S2009 did not require a component similar to L4, it is likely due to the fact that the LETG has lower sensitivity at short wavelengths than the HETG, hence may not have detected the lines from ions such as Mg XII, Si XIV that were fit by including L4. Also, while we identified S2 with UV component 5, there is no corresponding component required in the HETG analysis. However, it is possible, given the uncertainties in velocities, that L2 could correspond to either S1, as we suggested above, or S2. This is most likely evidence of the difficulty in deconvolving relatively low-ionization components of absorption, with radial velocities  $\lesssim$  a few  $100 \text{ km s}^{-1}$  of each other, solely based on the analysis of X-ray spectra. While S2009 did not require a component similar to L3a, and the relative constancy of the UV absorbers is evidence against temporal variations, since L3a has no strong UV signature, it is possible that it was weaker during the LETG observations. Finally, there was no evidence for low-



velocity, low-ionization gas, i.e., L1, in the LETG spectrum. In the latter case, the models for UV components 8 and 9 do not predict significant X-ray absorption (see Table 5), hence it is likely that the differences are due to the parametrization of the black-body component, as suggested above.

As noted in Section 1, one possible acceleration mechanism for mass outflows is radiation pressure. Radiative driving requires that the inverse of the ratio of the luminosity of source to its Eddington limit,  $L/L_{\text{Edd}}$ , exceeds the force multiplier ( $FM$ ), or ratio of the total photo-absorption cross-section, including bound-free and bound-bound transitions, to the Thomson cross-section (e.g. Arav et al. 1994). For UV components 2, 5, and 7, the values of  $FM$ , at the illuminated face, are  $1.57 \times 10^2$ ,  $1.35 \times 10^2$ , and  $1.81 \times 10^2$ , respectively. Based on the estimated bolometric luminosity,  $L_{\text{bol}} = 10^{43}$  ergs  $\text{s}^{-1}$ , from Vasudevan & Fabian (2009),  $L_{\text{bol}}/L_{\text{Edd}} \sim 0.05$  for NGC 4051, hence, based on our models, each of these components could be radiatively-driven. For comparison, X-ray zones L3a and L3b have  $FM$  values of 16.8 and 9.7, respectively, which are marginally consistent with radiative driving, in particular if the central source were somewhat more luminous in the past. On the other hand, L4 has a  $FM = 1.9$ , which suggests another acceleration mechanism (see Section 1), unless the gas had been accelerated to its present velocity during a period in which the source was significantly more luminous. The difference in  $FM$  for L4 and UV component 2 suggests complex dynamical interactions, if these components are indeed co-located.

## 5.2. Radial Distances and Density Constraints

Both L2011 and S2009 derived constraints on the radial distances of the X-ray absorbers. Based on the assumption that the physical depths of the absorbers do not exceed their radial distances (which is a requirement for models that assume open geometry), L2011 obtained upper limits for the radial distances for their four lowest-ionization components components (see their Table 8). S2009 used the lack of variability to obtain lower limits for components S1, 3, and 4 (see their Table 5). For those components which were identified in both studies (see Table 6), the lower limits obtained by L2011, are consistent with the upper limits from S2009. Based on recombination time arguments, the decrease in ionization parameter for S2,, required by their modeling of the variations over a 20 ksec period, indicates a radial distance of  $\leq 3 \times 10^{17}$  cm, roughly consistent with the estimate for the lowest ionization component modeled by Krongold et al. (2007). Overall, this suggests that the limits on radial distances determined by S2009 are consistent with the other studies and can be used to constrain the radial distances and densities of the UV absorbers.

In Table 4, we list the estimated radial distances and densities, based on  $Q$  and  $U$ , for

the UV absorbers. As noted above, we have associated UV component 5 with S2. Using the upper limit for radial distance,  $r$ , from S2009,  $< 3 \times 10^{17}$  cm, we derive an lower limit for  $n_{\text{H}} < 7.9 \times 10^6 \text{ cm}^{-3}$ . Assuming UV component 7 and S1 are the same, for the lower limit if  $r > 9 \times 10^{17}$  cm, we derive an lower limit for  $n_{\text{H}} < 1.3 \times 10^6 \text{ cm}^{-3}$ . Although component 2 is much lower ionization than the X-ray components closest in radial velocity, S3 or L4, for the sake of comparison we may assume that it lies somewhere within the range of radial distances estimated by S2009, e.g.,  $r \sim 0.5\text{pc}$ . These estimates place each of these absorbers outside the region which we have defined as the ILR (see Section 2), but within much of the NLR, hence are consistent with the evidence that components 2, 5, and 7 do not cover the NLR, as discussed in Section 3. Assuming L4 is at the same radial distance as component 2,  $\log n_{\text{H}} = 3.28$ . The predicted gas pressures at the ionized face for component 2 and L4 are  $3.41 \times 10^{-6} \text{ dyne cm}^{-2}$  and  $2.73 \times 10^{-7} \text{ dyne cm}^{-2}$ , respectively. Therefore, these two components would not be in full pressure equilibrium and component 2 would expand and dilute over time, unless confined by some other physical process, e.g. magnetic confinement (see discussion in Gabel et al. 2005).

Based on the model parameters and distance constraints we can estimate the mass loss rates for the UV absorbers,  $\dot{M} = 8\pi r N_{\text{H}} m_{\text{p}} \mu v_{\text{r}} C_{\text{g}}$ , where the mean atomic mass per proton  $\mu = 1.43$  for solar abundances and  $C_{\text{g}}$  is the global covering fraction of the absorbers. We obtain the following rates: component 2,  $\sim 0.01 C_{\text{g}} M_{\odot} \text{ yr}^{-1}$ ; component 5,  $< 1.76 \times 10^{-3} C_{\text{g}} M_{\odot} \text{ yr}^{-1}$ ; component 7,  $> 1.37 \times 10^{-3} C_{\text{g}} M_{\odot} \text{ yr}^{-1}$ . The combined mass loss from these components is on the same order as the fueling rate ( $\approx 0.004 M_{\odot} \text{ yr}^{-1}$ ; Turner et al. 2010). However, as suggested by L2011, most of the mass loss is from the high ionization/high velocity component and components L3a and L4. Greater mass loss in more highly ionized gas than in the UV absorbers has been claimed for other AGN (e.g., NGC 5548; Crenshaw et al. 2009). This is suggestive of a scenario in which the UV absorbers are knots or condensations in a more highly ionized wind, with the bulk of the mass contained in the latter.

### 5.3. Relation to the Emission-line gas

Cecil et al. (2002) suggested that some components of the NLR emission-like gas in NGC 1068 would resemble intrinsic UV absorbers if viewed along the line-of-sight to the AGN. Crenshaw & Kraemer (2007) determined that emission lines from the ILR of NGC 4151 could arise in the same gas responsible for the UV and soft X-ray absorption. In photoionization modeling studies of the NLR in NGC 4151 (Kraemer et al. 2000), NGC 1068 (Kraemer & Crenshaw, 2000a; 2000b), Mrk 3 (Collins et al. 2009), and Mrk 573 (Kraemer et al. 2009),

in order to account for the strength emission lines such as [Ne V]  $\lambda 3426$  and [Fe V]  $\lambda 6087$ , we argued for the presence of relatively highly ionized, e.g.  $\log U \sim -1$ , matter-bounded gas within 50 pc of the AGN. Although the column densities of these components are typically several times greater than what we have determined for components 2, 5, and 7 in NGC 4051, they span the same range in  $U$ . Hence it is plausible that we are viewing the BLR/central source in NGC 4051 through gas in the inner regions of the NLR, in agreement with the determination of our line-of-sight based on the emission-line kinematics, which places our view at a polar angle of  $\sim 12^\circ$  with respect to the NLR bicone axis and through the NLR material (Fischer et al. 2011). Interestingly, as is the case in NGC 5548 (Crenshaw et al. 2009), we find no evidence that the ILR is viewed in absorption, which suggests that the ILR is located at relatively larger polar angle.

## 6. Summary

As part of a coordinated program, including *Chandra*/HETG and *Suzaku* observations, to study the nature of intrinsic absorption in the NLSy1 NGC 4051, we have obtained and analyzed new COS spectra. Based on the spectral analysis and photoionization modeling, we have determined the following:

1. We detect the same components of UV absorption identified in STIS spectra by Collinge et al. (2001). None of the absorbers have shown clear changes in column density or kinematic profiles, which indicates the absorption lines of H I, N V and C IV in the strongest components, 2, 5, and 7, are saturated, while the weaker components have low densities and, hence, have not responded to changes in the ionizing flux over the  $\sim 10$  years separating the the STIS and COS observations..

2. Of the UV kinematic components, 2 – 7 (and possibly 1) are associated with mass outflow. Based on photoionization modeling, we identified component 5 as zone 4 from the analysis of the LETG spectrum by S2009. Component 7 is likely the same zone 1 from S2009, and zone 2 from our analysis of the HETG spectra, although the line widths required by the X-ray analyses indicate a by a second component, which we suggest is component 6. Most of the UV components are likely to be clumps in a more highly ionized, lower density wind associated with the X-ray absorbers.

3. The predicted force multipliers for the three strongest UV components, 2, 5, and 7, exceed the inverse of  $L_{\text{bol}}/L_{\text{Edd}}$  for NGC 4051, hence it is plausible that they have been accelerated by radiation pressure. On the other hand, we find that X-ray component L4 may be too highly ionized to be radiatively driven, which suggests a complex interaction with

UV component 2 if they are co-located.

4. The combined mass loss rate from these UV components is  $\approx 0.01 C_g M_\odot \text{ yr}^{-1}$ , which is on the same order as the estimated fueling rate. Nevertheless, as discussed in L2011, the mass loss is dominated by the contributions from more highly ionized absorbers, hence it is likely that the total mass loss rate significantly exceeds the fueling rate.

5. As in the case of NGC 5548 (Crenshaw et al. 2009), there is no evidence that the UV absorbers are associated with the ILR. Rather, the ionization parameters and column densities determined for components 2, 5, and 7 are in the range of those found for relatively high ionization gas in multi-component modeling of the NLR in several Seyfert galaxies. This suggests that we are viewing the AGN in NGC 4051 through the NLR gas, in agreement with the geometry derived from kinematic modeling (Fischer et al. 2011) and the constraints on the radial distances of the UV absorbers.

Support for program 11834 was provided by NASA through a grant from the Space Telescope Science Institute, which is operated by the Association of Universities for Research in Astronomy, Inc., under NASA contract NAS 5-26555. This research has made use of the NASA/IPAC Extragalactic Database (NED) which is operated by the Jet Propulsion Laboratory, California Institute of Technology, under contract with the National Aeronautics and Space Administration. This research has made use of NASA’s Astrophysics Data System Bibliographic Services. Some/all of the data presented in this paper were obtained from the Multimission Archive at the Space Telescope Science Institute (MAST). Support for MAST for non-HST data is provided by the NASA Office of Space Science via grant NNX09AF08G and by other grants and contracts. We thank Gary Ferland for his continued maintenance of the code Cloudy.

## REFERENCES

- Ali, B., Blum, R.D., Bumgardner, T.E., Cranmer, S.R., Ferland, G.J., Haefner, R.I., & Tiede, G. P. 1991, *PASP*, 103, 1182
- Arav, N., Li, Z.-Y., & Begelman, M.C. 1994, *ApJ*, 432, 62
- Asplund, M., Grevesse, N., Sauval, A.J., & Scott, P. 2009, *ARA&A*, 47, 481
- Blandford, R. D., & Payne, D.G. 1982, *MNRAS*, 199, 883
- Begelman, M. C., McKee, C. F., & Shields, G. A. 1983, *ApJ*, 271, 70
- Bowen, D.V., et al. 2008, *ApJS*, 176, 59
- Cecil, G., Dopita, M.A., Groves, B., Wilson, A.S., Ferruit, P., Pecontel, E., & Binette, L. 2002, *ApJ*, 568, 627
- Chelouche, D., & Netzer, H. 2005, *ApJ*, 625, 95
- Collinge, M.J., et al. 2001, *ApJ*, 557, 2
- Collins, N.R., Kraemer, S.B., Crenshaw, D.M., Bruhweiler, F.C., & Meléndez, M. 2009, *ApJ*, 694, 765
- Crenshaw, D.M., & Kraemer, S.B. 2007, *ApJ*, 659, 250
- Crenshaw, D.M., Kraemer, S.B., & Gabel, J.R. 2004, in *AGN Physics with the Sloan Digital Sky Survey*, ed. G.T. Richards & P.B. Hall (San Francisco: Astronomical Society of the Pacific), *ASP Conference Series*, 311, 235
- Crenshaw, D.M., Kraemer, S.B., & George, I.M. 2003, *ARA&A*, 41, 117
- Crenshaw, D.M., Kraemer, S.B., Schmitt, H.R., Kaastra, J.S., Arav, N., Gabel, J.R., & Korista, K.T. 2009, *ApJ*, 698, 281
- Crenshaw, D.M., Kraemer, S. B., Boggess, A.; Maran, S. P., Mushotzky, R. F., & Wu, C.-C. 1999, *ApJ*, 516, 750
- Denney, K.D., et al., 2009, *ApJ*, 702, 1353
- deVaucouleurs, G., deVaucouleurs, A. Corwin, H.G., Jr., Buta, R.J., Paturel, G., & Fouqué, P. 1991, *Third Reference Catalogue of Bright Galaxies* (New York: Springer)
- Dixon, W.V., et al. 2010, *Cosmic Origins Spectrograph Instrument Handbook, Version 2.0* (Baltimore: STScI)
- Dunn, J.P., Crenshaw, D.M., Kraemer, S.B., & Gabel, J.R. 2007, *AJ*, 134, 1061
- Dunn, J.P., Crenshaw, D.M., Kraemer, S.B., & Trippe, M.L. 2008, *AJ*, 136, 1201
- Dunn, J.P., Jackson, B., Deo, R.P., Farrington, C., Das, V., & Crenshaw, D.M. 2006, *PASP*, 188, 572

- Fischer, T., Crenshaw, D.M., Kraemer, S.B., & Schmitt, H.R. 2011, "Narrow-Line Seyfert 1 Galaxies and their place in the Universe", ed., L. Foschini, M. Colpi, L. Gallo, D. Grupe, S. Komossa, K. Leighly, & S. Mathur, published online at <http://pos.sissa.it/cgi-bin/reader/>
- Fox, A.J., Savage, B.D., & Wakker, B.P. 2006, *ApJS*, 165, 229
- Gabel, J.R., et al. 2005, *ApJ*, 631, 741
- Green, J.C., et al. 2012, *ApJ*, 744, 60
- Guainazzi, M., Mihara, T., Otani, C., & Matsuoka, M. 1996, *PASJ*, 48, 781
- Kaastra, J.S., Mewe, R., Liedahl, D.A., Komossa, S., & Brinkman, A. C. 2000, *A&A*, 354, L83
- Kaspi, S., Brandt, W.N., Collinge, M.J., Elvis, M., & Reynolds, C.S. 2004, *AJ*, 127, 2631
- Kaspi, S., Brandt, W. N., Netzer, H., Sambruna, R., Chartas, G., Garmire, G. P., & Nousek, J. A. 2000, *ApJ*, 535, L17
- Komossa, S., & Fink, H. 1997, *A&A*, 332, 719
- Kraemer, S.B., & Crenshaw, D.M., 2000a, *ApJ*, 532, 256
- Kraemer, S.B., & Crenshaw, D.M., 2000b, *ApJ*, 544, 736
- Kraemer, S.B., Crenshaw, D.M., George, I.M., Netzer, H., Turner, T.J., & Gabel, J.R. 2002, *ApJ*, 577, 98
- Kraemer, S.B., Crenshaw, D.M., Hutchings, J.B., Kaiser, M.E., Nelson, C.H., & Weistrop, D. 2000, *ApJ*, 531, 278
- Kraemer, S.B., Crenshaw, D.M., Trippe, M.L., Meleéndez, M., Schmitt, H.R., & Fischer, T.C. 2009, *ApJ*, 698, 106
- Kraemer, S. B., Crenshaw, D. M., Yaqoob, T., McKernan, B., Gabel, J. R., George, I. M., Turner, T. J., & Dunn, J.P. 2003, *ApJ*, 582, 125
- Kraemer, S.B. et al. 2006, *ApJS*, 167, 161
- Kraemer, S.B., et al. 2005, *ApJ*, 633, 693
- Kraemer, S.B., et al. 2001, *ApJ*, 551, 671
- Kriss, G.A., et al. 1996, *ApJ*, 467, 629
- Kriss, G.A., et al. 2000, *ApJ*, 538, L17
- Krolik, J.H., & Kriss, G.A., 2001, *ApJ*, 561, 684
- Krongold, Y., Nicastro, F., Elvis, M., Brickhouse, N., Binette, L., Mathur, S., & Jiménez-Bailón, E. 2007, *ApJ*, 659, 1022

- Leighly, K.M. 1999, *ApJS*, 125, 297
- Lobban, A.P., Reeves, J.N., Miller, L., Turner, T.J., Braitto, V., Kraemer, S.B., & Crenshaw, D.M. 2011, *MNRAS*, 414, 1995
- Mathur, S., 2000, *MNRAS*, 314, L17
- Mathur, S., Elvis, M., & Wilkes, B. 1999, *ApJ*, 519, 605
- Meléndez, M., Kraemer, S.B., Weaver, K.A., & Mushotzky, R.F. 2011, *ApJ*, 738, 6
- Miller, L., Turner, T.J., Reeves, J.N., Lobban, A., Kraemer, S.B., & Crenshaw, D. M. 2010, *MNRAS*, 403, 196
- Murray, N., Chiang, J., Grossman, S. A., & Voit, G. M. 1995, *ApJ*, 451, 498
- Osterbrock, D.E., & Pogge, R.W. 1985, *ApJ*, 297, 166
- Peterson, B.M., et al. 2004, *ApJ*, 613, 682.
- Rees, M.J. 1987, *MNRAS*, 228, 47P
- Russel, D.G., 2004, *ApJ*, 607, 241
- Savage, B.D. & Mathis, J.S. 1979, *ARA&A*, 17, 73
- Scott, J.E., Arav, N., Gabel, J.R.; Kriss, G.A.; Quijano, J.K., Kaastra, J.S., Costantini, E., & Korista, K. 2009, *ApJ*, 694, 438
- Scott, J.E., et al. 2005, *ApJ*, 624, 193
- Seaton, M.J. 1978, *MNRAS*, 185, 5P
- Shull, J.M. & van Steenberg, M.E. 1985, *ApJ*, 294, 599
- Shull, J.M., Jones, J.R., Danforth, C.W., & Collins, J.A. 2009, *ApJ*, 699, 754
- Srianand, R., & Petitjean, P. 2000, *A&A*, 357, 414
- Steenbrugge, K.C., Fenovcik, M., Kaastra, J.S., Costantini, E., & Verbunt, F. 2009, *A&A*, 496, 107 (S2009)
- Steenbrugge, K.C., et al. 2005, *A&A*, 434, 569
- Turner, T. J., George, I. M., Nandra, K., & Turcan, D. 1999, *ApJ*, 524, 667
- Turner, T.J., Kraemer, S.B., George, I.M., Reeves, J.N., & Bottorff, M.C. 2005, *ApJ*, 618, 155
- Turner, T. J., Miller, L., Kraemer, S. B., & Reeves, J. N. 2011, *ApJ*, 733, 48
- Turner, T.J., Miller, L., Reeves, J.N., Lobban, A., Braitto, V., Kraemer, S.B., & Crenshaw, D.M. 2010, *ApJ*, 712, 209
- Vasudevan, R.V., & Fabian, A.C. 2009, *MNRAS*, 392, 1124

Véron-Cetty, M.-P., Véron, P., & Goncalves, A. C. 2001, *A&A*, 372, 730

Wakker, B.P. 2006, *ApJS*, 163, 282

Wang, J.-M., & Netzer, H, 2003, *A&A*, 398, 927



Fig. 1.— Combined COS spectrum of NGC 4051 in the observed frame, smoothed with a 7-point boxcar. Prominent emission lines are labeled.

Fig. 2.— UV continuum light curve of NGC 4051. Fluxes at 1365 Å are plotted as a function of Julian date. The symbols are as follows: pluses – *IUE*, triangle – STIS, diamond – COS. Vertical lines indicate the one-sigma uncertainties.

Fig. 3.— Kinematic components of absorption for high-ionization lines in the UV spectrum of NGC 4051, originally identified by Collinge et al. (2001). The black line gives the COS spectrum and the red line gives the STIS spectrum. Fluxes are plotted as a function of radial velocity for the strongest member of each doublet, relative to an emission-line redshift of  $z = 0.002295$ . The kinematic components are identified for both members of each doublet.

Fig. 4.— Kinematic components of absorption for low-ionization lines in the UV spectrum of NGC 4051. The black line gives the COS spectrum and the red line gives the STIS spectrum. Fluxes are plotted as a function of radial velocity for each line, relative to an emission-line redshift of  $z = 0.002295$ .

Fig. 5.— Comparison of the C IV profiles from the COS (black line) and STIS spectra (red dashed line). The latter has been convolved with the COS LSF and scaled by a factor of 0.75. The only clear difference is excess emission in some of the absorption troughs, which is due to uncovered emission as described in the text.

Fig. 6.— COS Spectrum of the He II  $\lambda 1640$  region and continuum plus emission-line fits. Components of the fits are: continuum (dotted-dashed green line), continuum + BLR (dotted-dashed red line), continuum + BLR + ILR (dashed red line), and continuum + BLR + ILR + NLR (solid blue line).

Fig. 7.— Intrinsic absorption components in the COS spectrum as in Figure 3 and continuum plus emission-line fits. Components of the fits are: continuum (dotted-dashed green line), continuum + BLR (lower dashed red line), continuum + BLR + ILR (upper dashed red line), and continuum + BLR + ILR + NLR (dashed blue line). The dotted-dashed blue line shows a model for the uncovered emission in the intrinsic absorption components, which consists of the excess UV continuum flux discussed in the text plus the NLR emission.

Fig. 8.— Separate and combined normalized fluxes for components 2 (red), 5 (green), and 7 (blue), plotted against velocity. The broad, square-troughed combined profile (shown in black) resembles the O VI  $\lambda 1032$  profile from Kaspi et al. (2004) and spans the same range in velocity.

Fig. 9.— Comparison of the N V  $\lambda 1240$  and C IV  $\lambda 1550$  regions, from the COS spectrum,

showing the velocities of the individual UV absorption components, with the O VIII 1s-2p (18.96 Å) and O VII 1s-2p (21.60 Å) absorption profiles. The oxygen profiles were generated from the *Chandra*/MEG data, with the O VII binned up by a factor of 2, relative to O VIII, due to the lower S/N at those energies. The oxygen profiles have been shifted by  $-200 \text{ km s}^{-1}$  (see discussion in text). The strongest O VII absorption occurs near the velocities of UV components 2 and 7/8, while that of O VIII is coincident with UV component 2.

Fig. 10.— Simulation of components 6 (blue solid) and 7 (red solid), assuming  $\tau = 10$  in their cores, binned as follows: black solid- total profile; black dotted - binned to  $50 \text{ km s}^{-1}$  resolution; black dashed - smoothed to *Chandra*/LETG resolution of  $300 \text{ km s}^{-1}$ . The latter gives a FWHM =  $250 \text{ km s}^{-1}$ , similar to zone 4 in Steenbrugge et al.(2009), while the unsmoothed is  $160 \text{ km s}^{-1}$

Table 1. COS High-Resolution Spectra of NGC 4051

Grating	Wavelength Coverages (Å)	Exposure Time (s)
G130M	1137 – 1274, 1291 – 1429	1832
G130M	1156 – 1293, 1310 – 1449	2771
G160M	1389 – 1558, 1574 – 1748	2771
G160M	1412 – 1580, 1601 – 1772	2771

Table 2. Kinematic Absorption Components

Component	$v_r$ (km s <sup>-1</sup> )	FWHM (km s <sup>-1</sup> )
G	–727	74
1	–647	40
2	–505	165
3	–430	63
4	–337	52
5	–268	133
6	–158	45
7	–107	64
8 <sup>a</sup>	–48	84
9	+30	23

<sup>a</sup>Collinge et al. (2001) call the low-ionization gas at slightly more negative velocities Component 10.

Table 3. Ionic Column Densities in NGC 4051 ( $10^{14}$  cm $^{-2}$ )

$N_{ion}$	Component				
	2	5	7	8	9
H I	13±5	45±13		>960 <sup>a</sup>	
N V	>13.7	>10.6	>3.4	0.28±0.09	<0.1
C IV	>7.5	>7.3		>9.9 <sup>b</sup>	0.16±0.04
C III	0.3±0.1:	0.3±0.1		>2.5 <sup>a</sup>	
C II	—	—		>4.8 <sup>b</sup>	0.20±0.05
Si IV	<0.1	<0.1	<0.1	0.75±0.13	0.05±0.02
Si III	—	—		>0.46 <sup>b</sup>	0.019±0.005
Si II	—	—		>0.44 <sup>b</sup>	0.04±0.01
Fe II	—	—		0.49±0.21 <sup>a</sup>	<0.21

<sup>a</sup>Includes contributions from Component 7 and 9

<sup>b</sup>Includes contributions from Components 7

Table 4. Photoionization Model Parameters

Component	$\log U^a$	$\log N_{\text{H}}^a$	radial distance(pc)	$\log n_{\text{H}}^a$
2	−0.72	20.17	0.50 <sup>b</sup>	5.57
5	−0.64	20.40	<0.09 <sup>b</sup>	>6.90
7	−0.80	20.18	>0.29 <sup>b</sup>	<6.13
8H <sup>c</sup>	−2.40	19.0	> 1.25 × 10 <sup>4</sup>	< −1.52
8L <sup>c</sup>	−3.50	18.8	> 1.25 × 10 <sup>4</sup>	< −0.44
9 <sup>c</sup>	−2.78	17.7	> 1.93 × 10 <sup>4</sup>	< −0.44

<sup>a</sup> $N_{\text{H}}$  in units of  $\text{cm}^{-2}$ ;  $n_{\text{H}}$  in units of  $\text{cm}^{-3}$ . Note, while the values of  $U$  and  $N_{\text{H}}$  are those that yield the column densities listed in Table 5, the uncertainties in these parameters are an order of magnitude greater than the least significant figures quoted (see discussion in Section 4.2).

<sup>b</sup>based on constraints from Steenbrugge et al. (2009).

<sup>c</sup>see discussion in text.

Table 5. Predicted Ionic Column Densities<sup>a</sup> ( $10^{14}$  cm<sup>-2</sup>)

$N_{ion}$	Component					
	2	5	7	8H	8L	9
H I	26.2	36.6	32.6	149	$1.44 \times 10^3$	19.9
O VIII	23.0	52.5	17.3	—	—	—
O VII	411	764	375	—	—	—
O VI	198	299	224	0.19	—	—
C IV	6.62	8.39	9.14	7.21	0.10	0.16
C III	0.40	0.43	0.64	16.1	9.62	1.03
C II	—	—	—	0.79	7.21	0.13
N V	10.1	13.8	12.8	0.33	—	—
Si IV	—	—	—	1.09	0.09	0.05
Si III	—	—	—	0.79	0.52	0.81
Si II	—	—	—	0.06	1.43	0.02
Fe II	—	—	—	—	0.27	—

<sup>a</sup>Blanks indicate predicted  $N_{ion} < 10^{12}$  cm<sup>-2</sup>.

Table 6. Comparison of X-ray and UV components

Component <sup>a</sup>	$v_r$ (km s <sup>-1</sup> )	FWHM (km s <sup>-1</sup> )	logU	log $N_{\text{H}}^b$	UV absorber
L3b	-620	467	0.56	20.7	comp 1?
S3	-600	90	0.86	20.8	comp 1?
L4	-510	467	1.57	21.4	comp 2?
L3a	-350	467	0.76	21.0	comp 4?
S2	-270	170	-0.64	20.4	comp 5
S1	-210	300	-1.2	20.1	comp 6?, 7
L2	-20	1175	-0.8	20.1	comp 6?, 7
L1	+20	467	-2.25	20.5	comp 8, 9?

<sup>a</sup>Model components “L” from Lobban et al. (2011) and “S” from Steenbrugge et al. (2009) (see Section 5.1). Values of  $v_r$  for Lobban et al. are shifted by +200 km s<sup>-1</sup>.

<sup>b</sup> $N_{\text{H}}$  in units of cm<sup>-2</sup>.

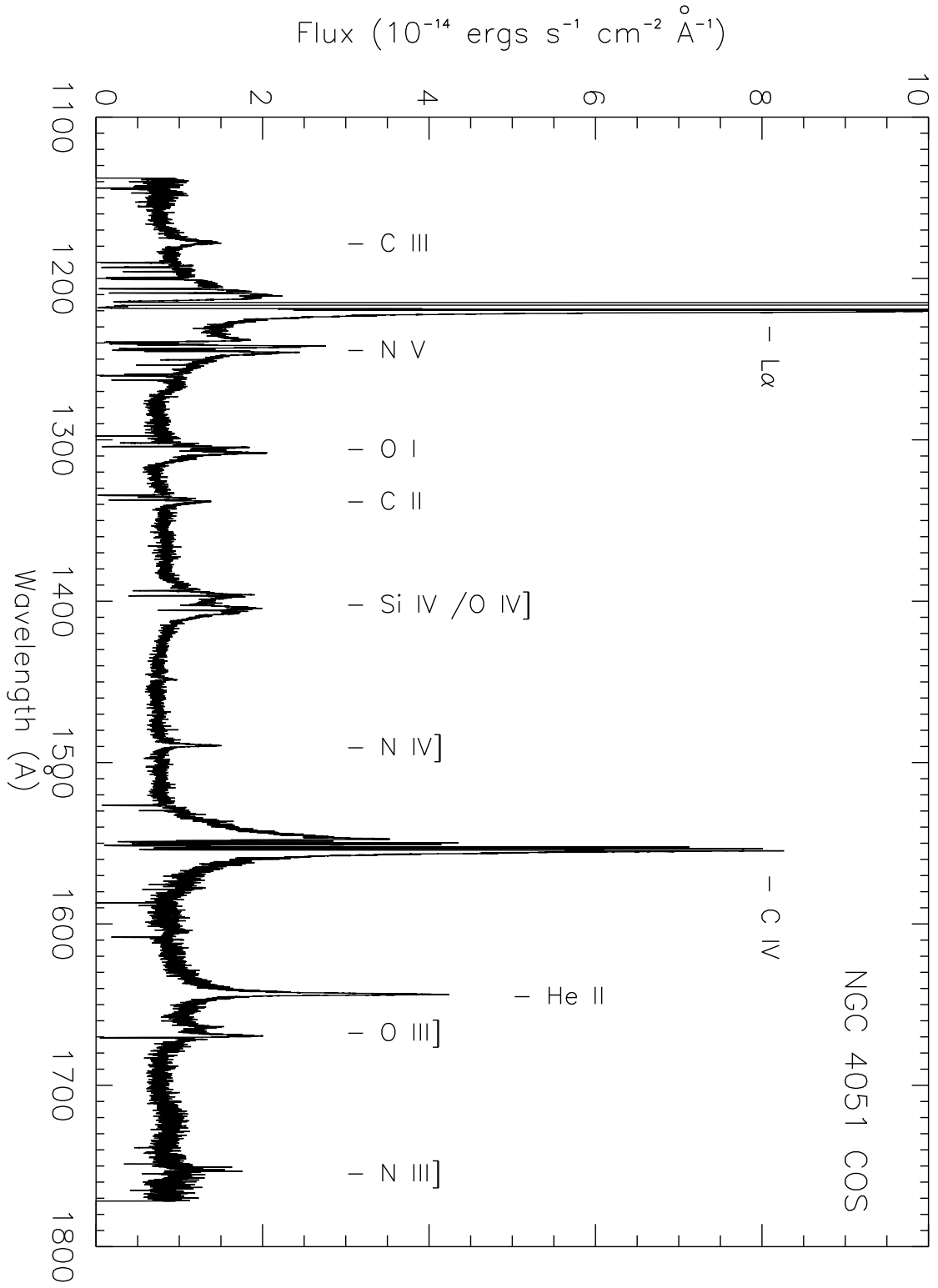


Fig. 1.





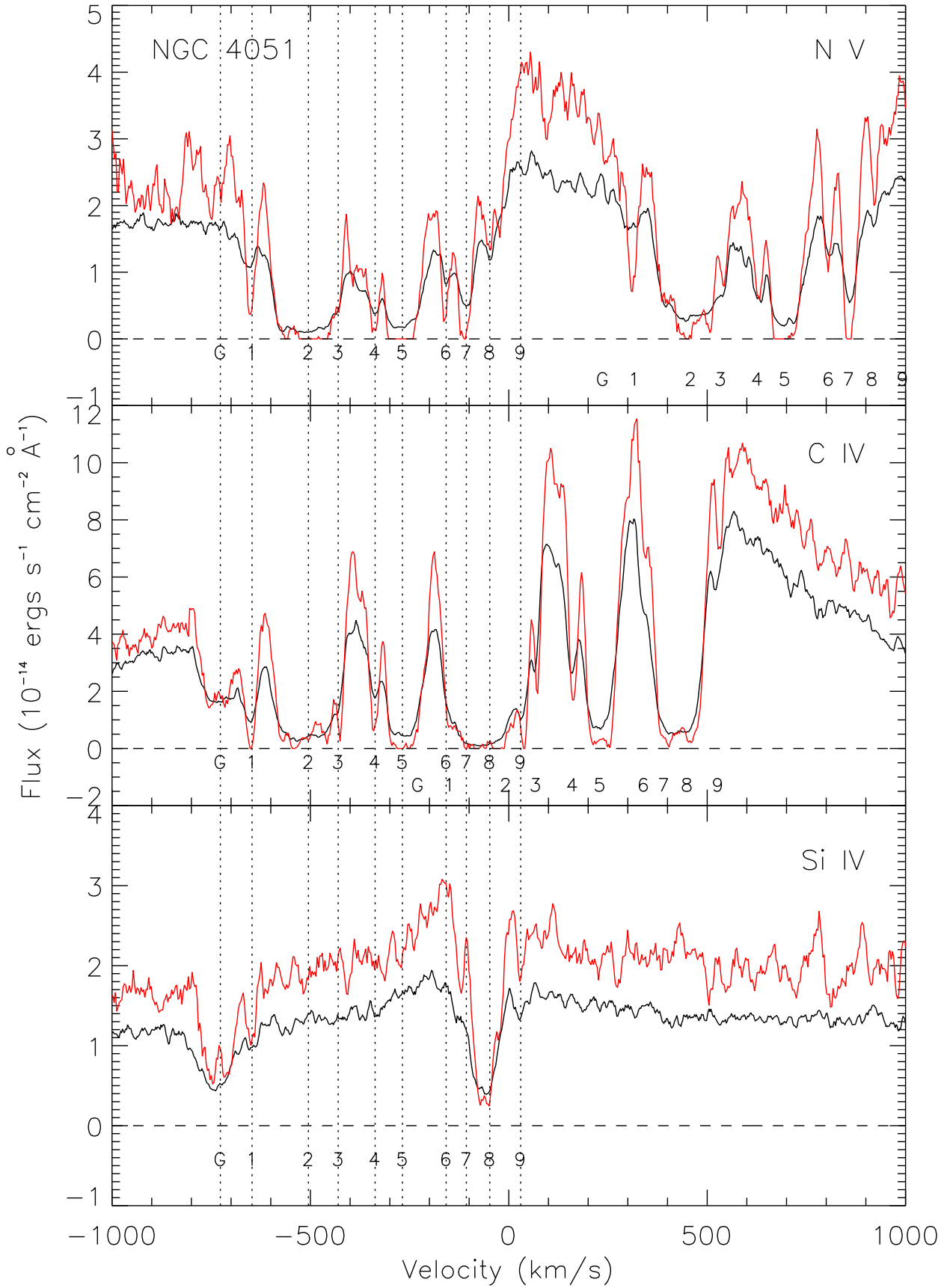


Fig. 3.

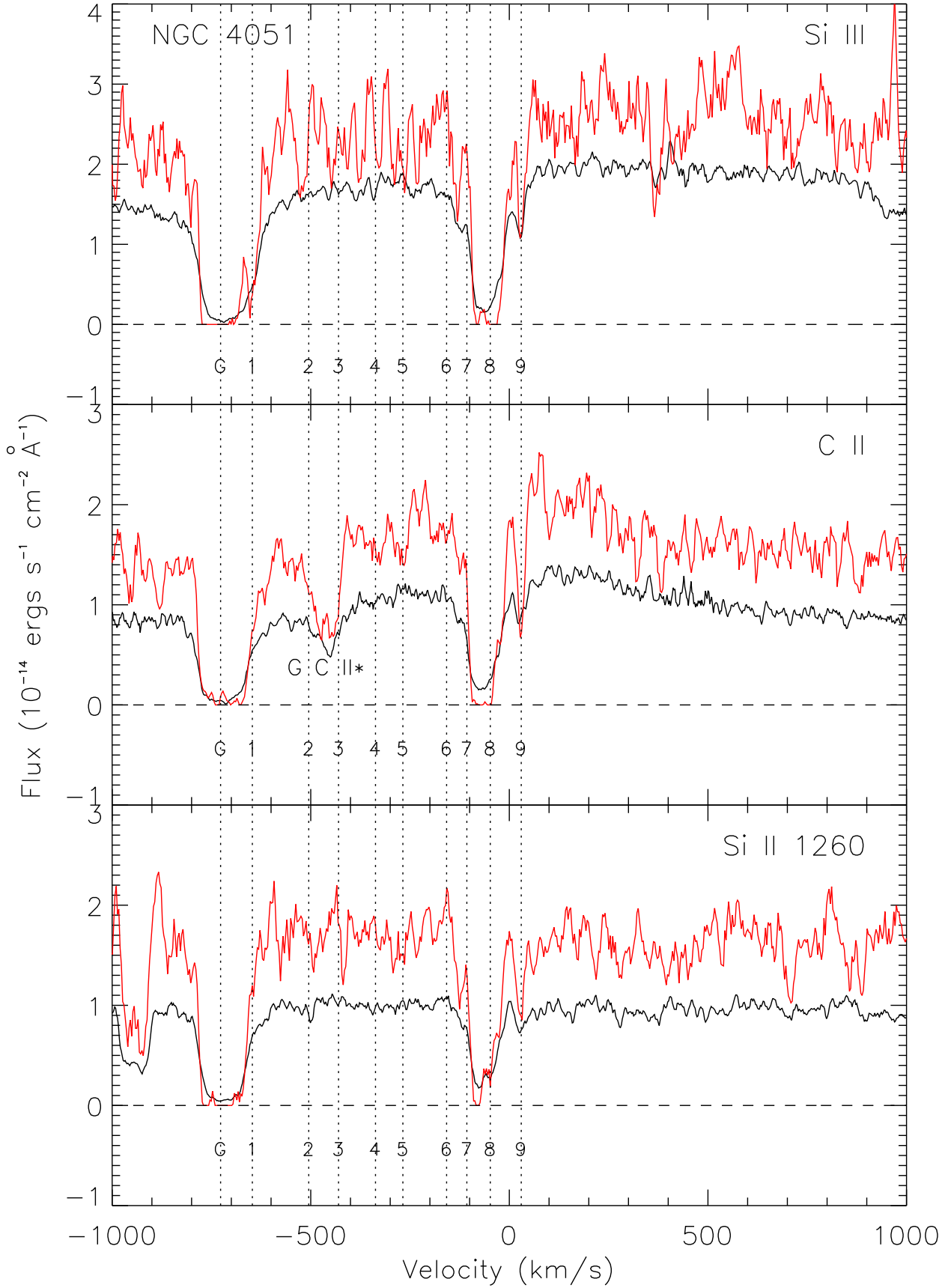


Fig. 4.

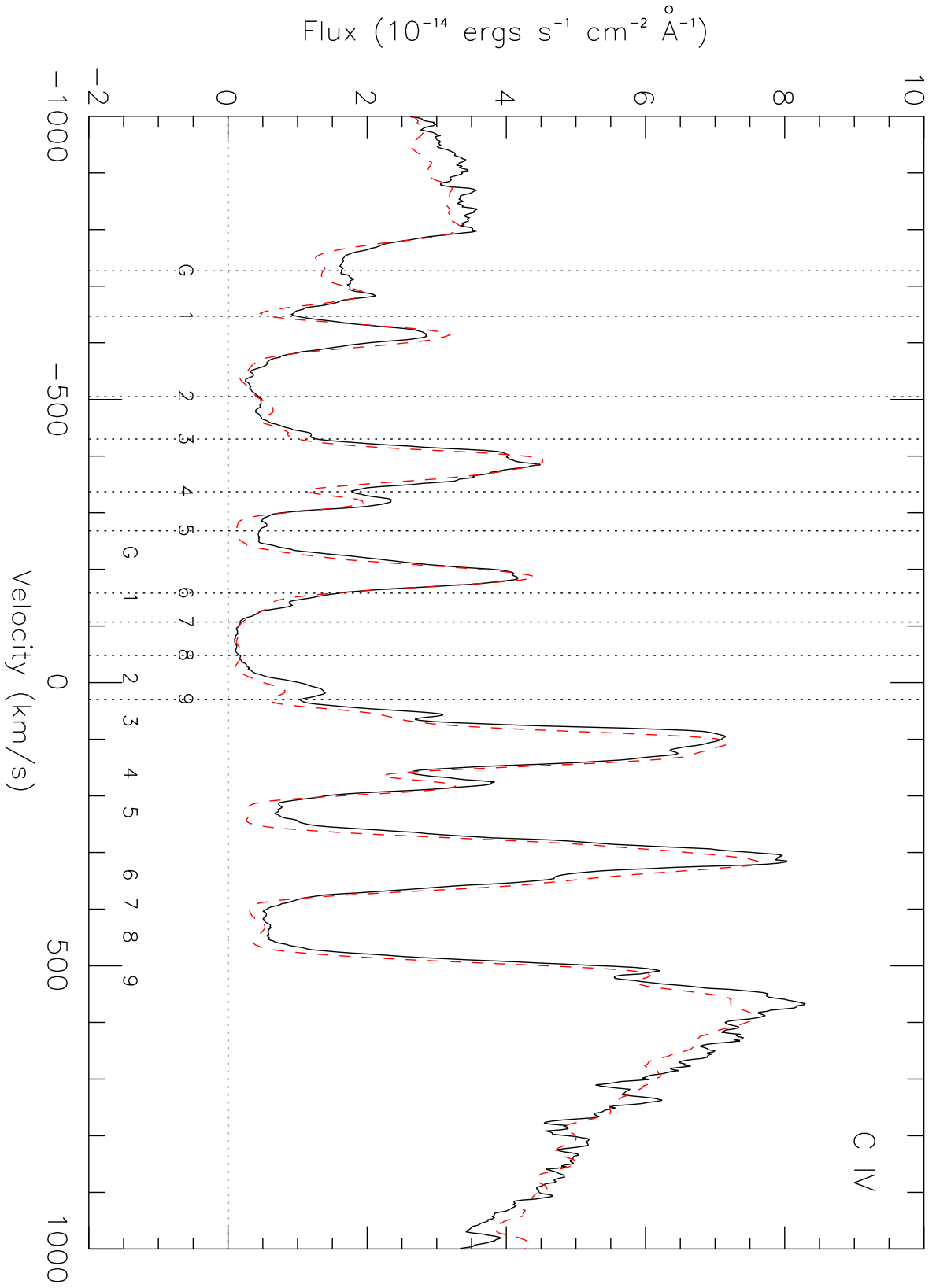


Fig. 5.

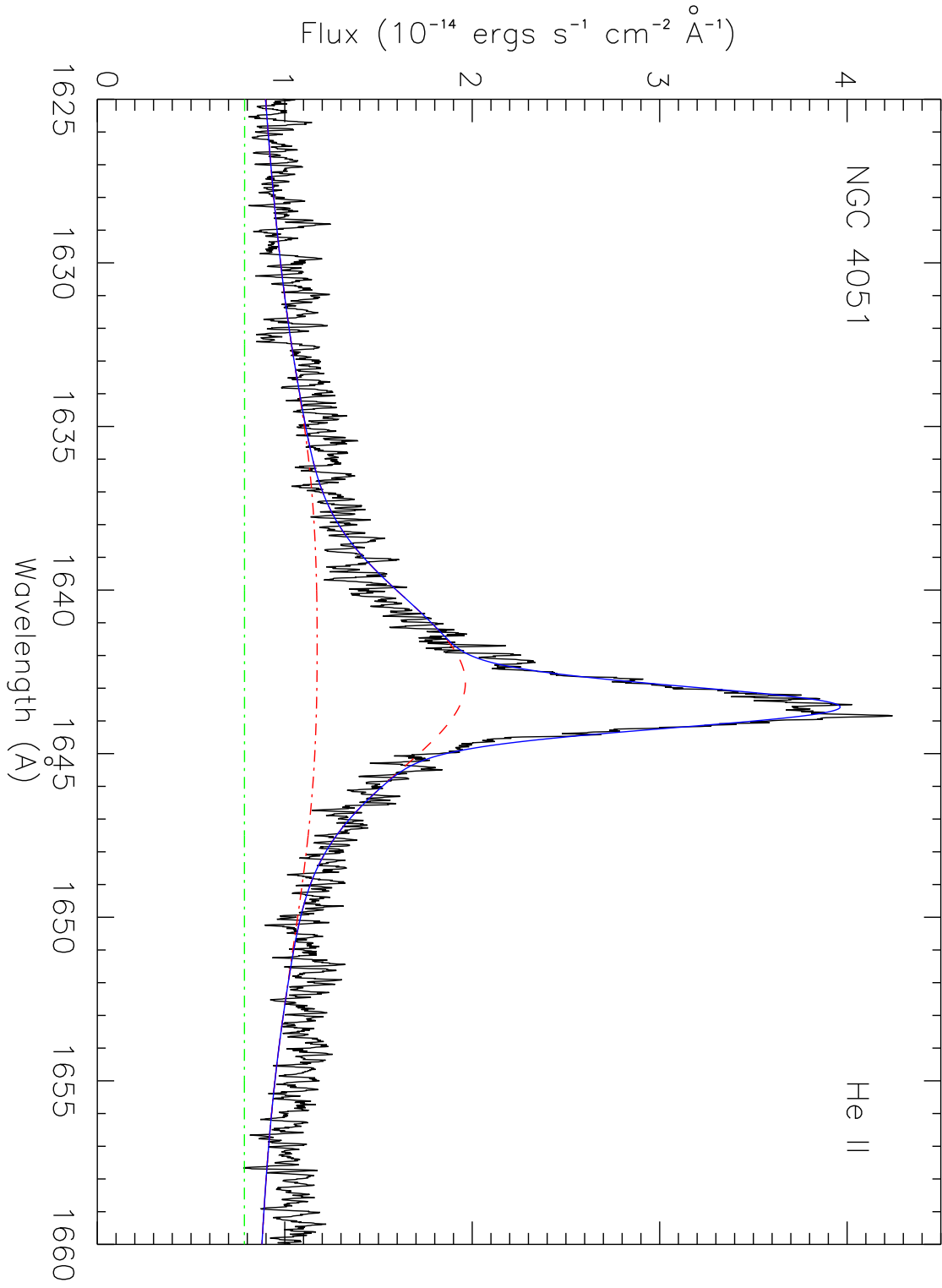


Fig. 6.

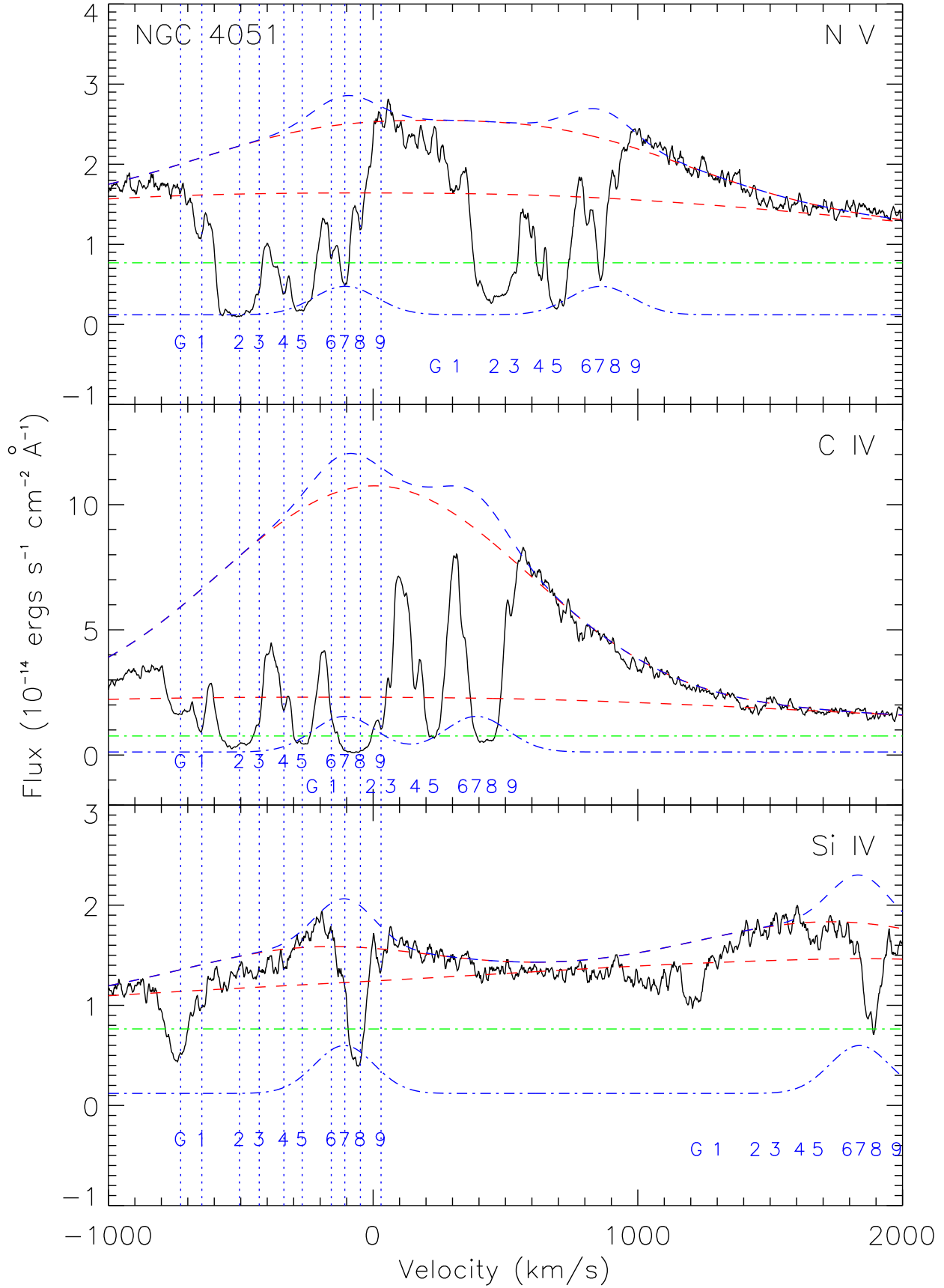


Fig. 7.

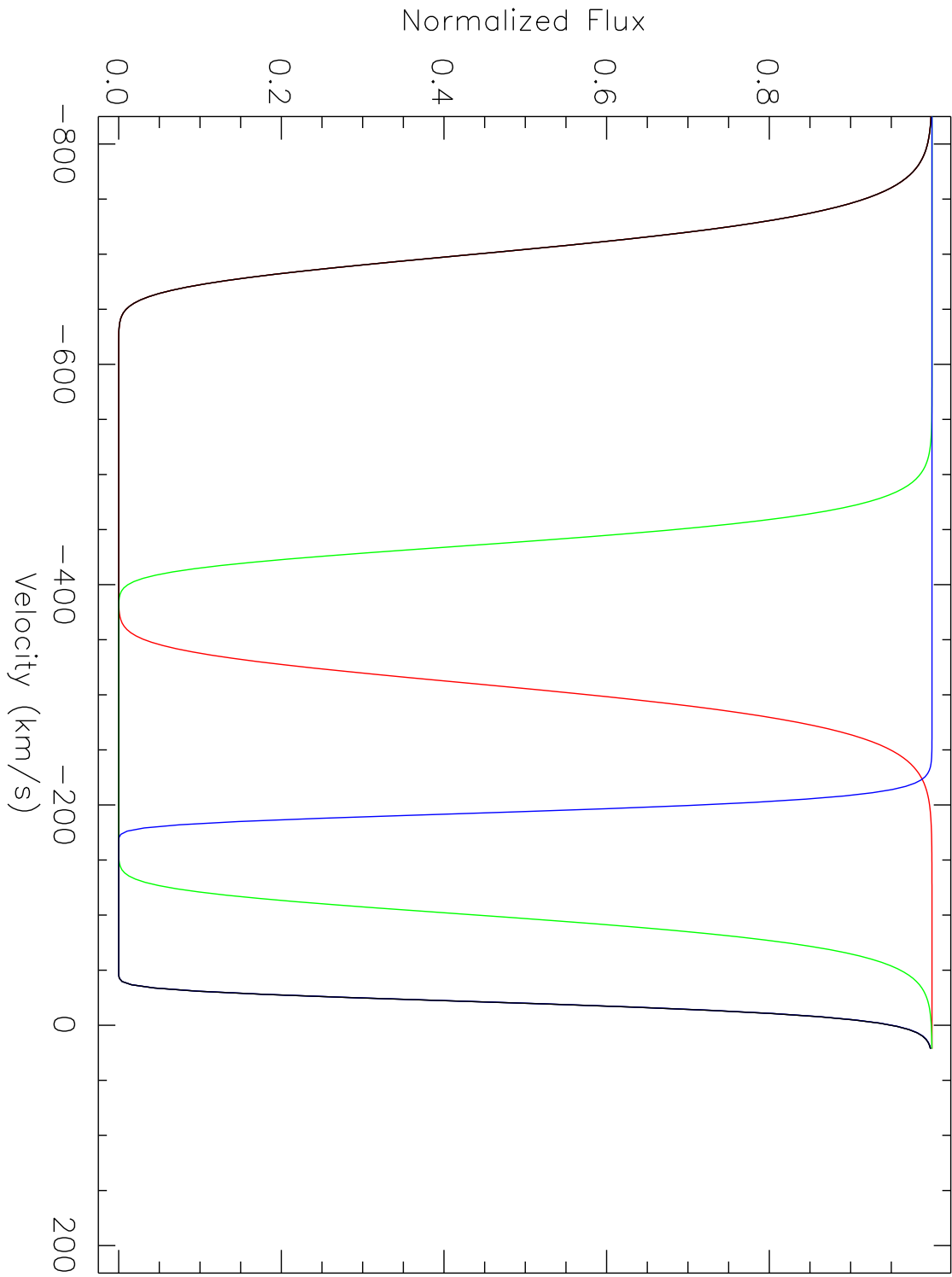


Fig. 8.

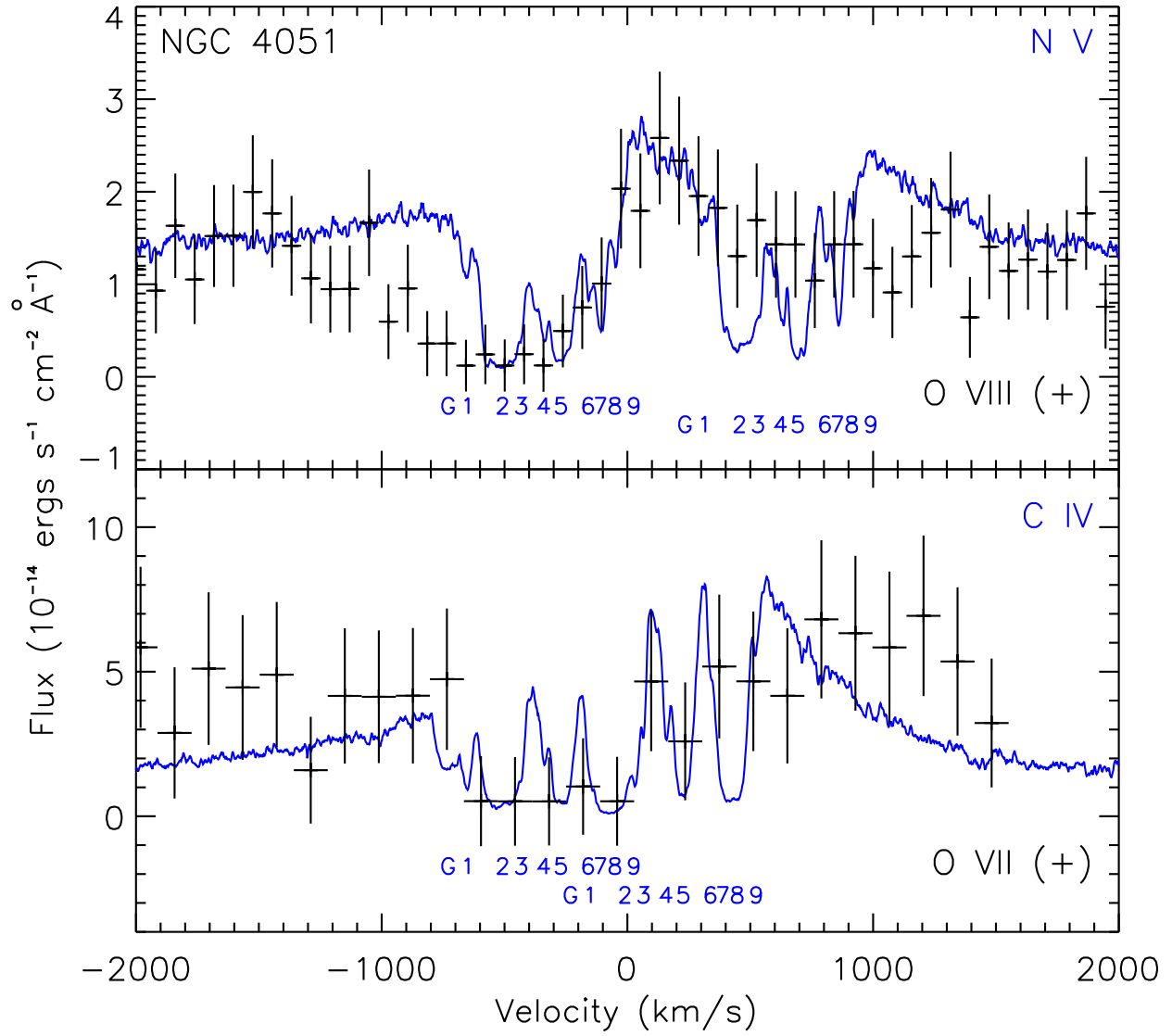


Fig. 9.



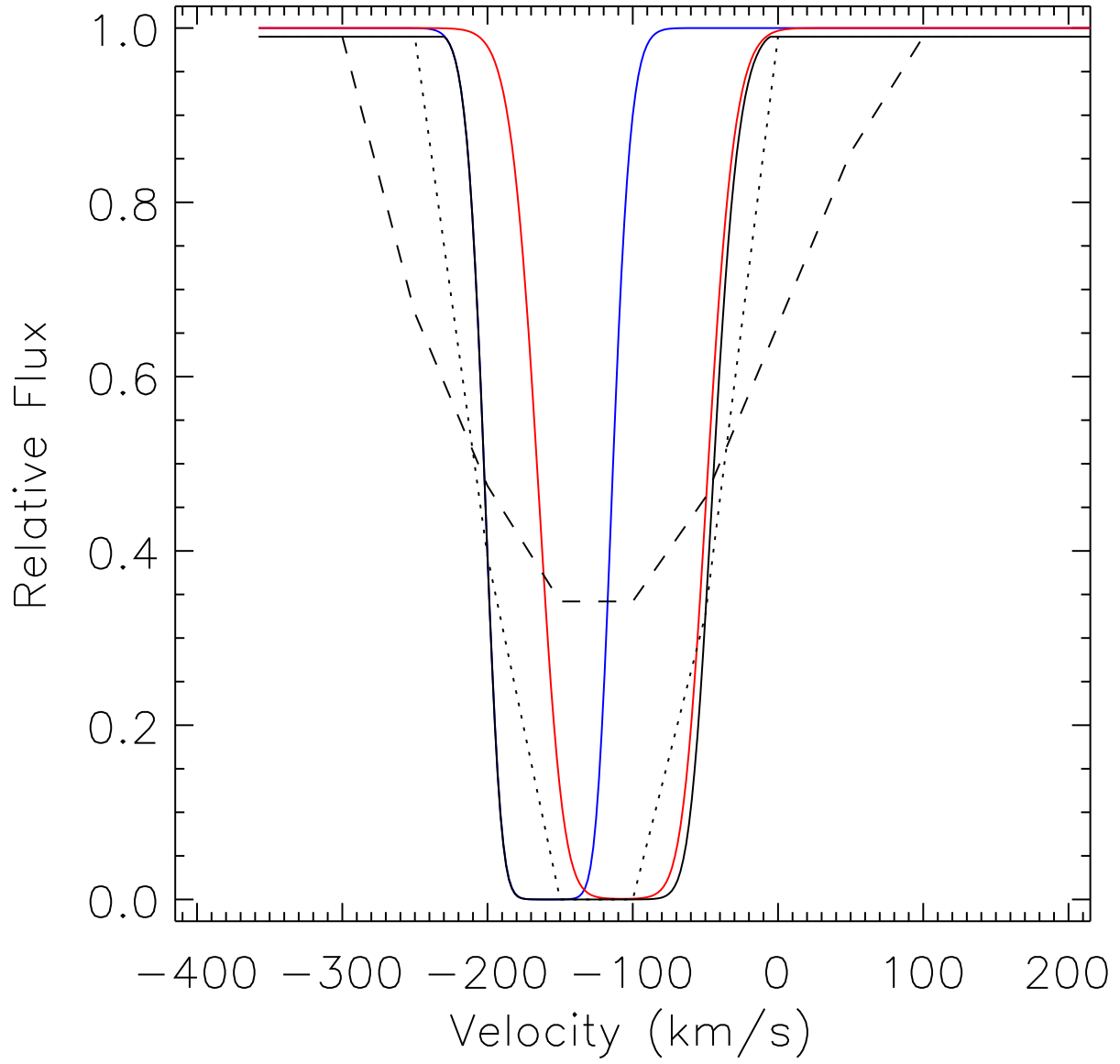


Fig. 10.